

1 **MHD study of extreme space weather conditions for exoplanets**
2 **with Earth-like magnetospheres: On habitability conditions and**
3 **radio-emission**

4 **J. Varela¹, A. S. Brun², P. Zarka³, A. Strugarek², F. Pantellini⁴, V. Réville⁴**

5 ¹Universidad Carlos III de Madrid, Leganes, 28911

6 ²Laboratoire AIM, CEA/DRF – CNRS – Univ. Paris Diderot – IRFU/DAP, Paris-Saclay, 91191 Gif-sur-Yvette Cedex,
7 France

8 ³LESIA & USN, Observatoire de Paris, CNRS, PSL/SU/UPMC/UPD/UO, Place J. Janssen, 92195 Meudon, France
9 ⁴LESIA, Observatoire de Paris, Université PSL, CNRS, Sorbonne Université, Université de Paris, 5 place Jules Janssen,

10 92195 Meudon, France

11 ⁵IRAP, Université Toulouse III—Paul Sabatier, CNRS, CNES, Toulouse, France

12 **Key Points:**

- 13 • Space weather
14 • Habitability conditions
15 • Radio emission
16 • M stars
17 • F stars

Corresponding author: J. Varela, jvrodri@fis.uc3m.es

Abstract

The present study aims at characterizing the habitability conditions of exoplanets with an Earth-like magnetosphere inside the habitable zone of M stars and F stars like τ Boo, caused by the direct deposition of the stellar wind on the exoplanet surface if the magnetosphere shielding is inefficient. In addition, the radio emission generated by exoplanets with a Earth-like magnetosphere is calculated for different space weather conditions. The study is based on a set of MHD simulations performed by the code PLUTO reproducing the space weather conditions expected for exoplanets orbiting the habitable zone of M stars and F stars type τ Boo. Exoplanets hosted by M stars at 0.2 au are protected from the stellar wind during regular and CME-like space weather conditions if the star rotation period is slower than 3 days, that is to say, faster rotators generate stellar winds and interplanetary magnetic fields large enough to endanger the exoplanet habitability. Exoplanets hosted by a F stars type τ Boo at ≥ 2.5 au are protected during regular space weather conditions, but a stronger magnetic field compared to the Earth is mandatory if the exoplanet is close to the inner edge of the star habitable zone (2.5 au) to shield the exoplanet surface during CME-like space weather conditions. The range of radio emission values calculated in the simulations are consistent with the scaling proposed by ? (?) during regular and common CME-like space weather conditions. If the radio telescopes measure a relative low radio emission signal with small variability from an exoplanet, that may indicate favorable exoplanet habitability conditions with respect to the space weather states considered and the intrinsic magnetic field of the exoplanet. The radio emission power calculated for exoplanets with an Earth-like magnetosphere inside the star habitable zone is in the range of $3 \cdot 10^7$ to $2 \cdot 10^{10}$ W if the space weather conditions lead to SW dynamic pressures between 1.5 to 100 nPa and IMF intensities between 50 - 250 nT, and is below the sensitivity threshold of present radio telescopes at parsec distances.

1 Introduction

The space weather effects on the Earth magnetosphere were extensively studied in the last years (? , ? , ? , ?), particularly during extreme events such as intense coronal mass ejections (CME) (? , ? , ?) leading to major perturbations in the Earth magnetosphere structures (? , ? , ? , ?).

The CMEs are solar eruptions produced in the corona due to magnetic reconnections, expelling fast charged particles and a magnetic cloud (? , ? , ? , ?). Extreme space weather events are not exclusive of the Sun or solar-like stars (? , ?), CMEs were also observed in M, K and F type stars (? , ? , ?).

The space weather at the orbit of the Earth and exoplanets depends on the stellar wind (SW) and interplanetary magnetic field (IMF) generated by the host star (? , ? , ?) at their orbital location as well as the conducting and magnetic properties of the local environment. For the case of the Earth, the intrinsic magnetic field is strong enough to avoid the direct precipitation of the SW on the surface even during the largest CMEs observed (? , ? , ? , ?). Extreme space weather conditions occur if the SW dynamic pressures in the range of the 10 to 100 nPa and IMF intensity between 100 and 300 nT.

The space weather in the orbit of exoplanets cannot be compared to the case of the Earth if the host star has characteristics different from the Sun (star type, age, metallicity, ...). If the SW dynamic pressure and IMF intensity generated by the star are large, favorable exoplanet habitability state requires an intrinsic magnetic field strong enough to avoid the direct precipitation of the SW on the exoplanet surface (? , ? , ? , ?). Otherwise, if the protection of the magnetic field is deficient, the exoplanet habitability can be hampered by the effect of the SW as well as the depletion of the atmosphere, especially volatile components such as the water molecules (? , ? , ? , ?). It should be noted that other important factors for the habitability as EUV, X ray and cosmic rays fluxes towards the exoplanet surface are not included in the analysis as such effects are beyond the scope of the present study. Nevertheless, the eventual direct precipitation of the SW must be understood as an important constraint for the habitability of planets.

Exoplanet habitability could be constrained for exoplanet without an intrinsic magnetic field, although the detection and characterization of exoplanet magnetospheres is a challenging topic. It is known from the interaction of the SW with the planets of the solar system that intrinsic magnetic fields are emitters of cyclotron MASER emission at radio wavelengths (ν , ν , ν , ν), generated by energetic electrons accelerated in the reconnection region between IMF and the planet magnetic field, flowing towards the planet surface along the magnetic field lines (ν , ν). A fraction of the electrons energy is transformed into cyclotron radio emission (ν , ν) escaping from the magnetosphere. Such radio emission is detected by ground-based radio telescopes, for example the Nançay decameter array (ν , ν), NenuFAR (ν , ν) and Low Frequency Array (LOFAR) (ν , ν) between others. Likewise, the radio emission detected from an exoplanet magnetosphere could provide information of the exoplanet intrinsic magnetic field (ν , ν). Unfortunately, the detection capability of present radio telescopes barely distinguish the radio emission from exoplanets. Recent LOFAR and the Australian Telescope Compact Array (ATCA) measurements tentatively achieved the detection of radio emission from exoplanet systems (ν , ν , ν). In addition, radio emission from the red dwarf GJ 1151 was measured, potentially originated in the magnetic interaction with a exoplanet with approximately the size of the Earth (ν , ν , ν , ν). Next generation of radio telescopes may be able to detect exoplanet radio emissions at a distances of 20 parsec (ν , ν , ν , ν , ν), for example the Square Kilometre Array (SKA) (ν , ν), depending on the space weather conditions generated by the host star and the properties of the exoplanet magnetic field.

This study is the continuation of a research activity dedicated to analyze numerically the interaction of the stellar wind with planetary magnetospheres, particularly the radio emission generation with respect to the space weather conditions and the properties of the planet intrinsic magnetic field. First, the radio emission from the Hermean magnetosphere was analyzed in ν (ν), showing the important role of the IMF intensity, IMF orientation and SW dynamic pressure on the radio emission generated. Then, ν (ν) was dedicated to study the radio emission from exoplanets with different intrinsic magnetic field configurations, identifying a critical dependency between magnetosphere topology and radio emission. Next, ν (ν) analyzed the effect of extreme space weather conditions on the Earth magnetosphere. The aim of the present study is to analyze the effect of the space weather conditions on the magnetosphere of exoplanets orbiting the habitable zone of M and F stars. In addition, the radio emission generated from the exoplanet magnetosphere is estimated. The analysis consist in a set of MHD simulations assuming the exoplanet magnetic field is identical to the Earth magnetic field, reproducing the space weather conditions inside the habitable zone of M and F stars.

This paper is structured as follows. Section 2 presents the description of the numerical model. Section 3 introduces the analysis of the space weather effects on the magnetosphere of exoplanet orbiting the habitable zone of M and F stars. Section 4 presents the characterization of the radio emission generated by exoplanets with an Earth-like magnetosphere during extreme space weather conditions. Section 5 discusses and concludes the analysis results.

2 Numerical model

This study is performed using the ideal MHD version of the open-source code PLUTO in spherical coordinates. The model calculates the evolution of a single-fluid polytropic plasma in the nonresistive and inviscid limit (ν , ν). A detailed description of the model equations, boundary conditions and upper ionosphere model can be found in (ν , ν).

The interaction of the SW with planetary magnetospheres can be studied using different numerical models; present study uses a single fluid MHD code (ν , ν , ν , ν , ν , ν). The validity of MHD code results were checked by comparing the simulation results with ground-based magnetometers and spacecraft measurements (ν , ν , ν , ν , ν). The study was performed using the single-fluid MHD code PLUTO in spherical 3D coordinates (ν , ν). The model was applied successfully to study the global structures of the Hermean magnetosphere (ν , ν , ν , ν ,

119 ?, ?), the radio emission from exoplanets (?, ?) and the effect of extreme space weather con-
 120 ditions on the Earth magnetosphere (?, ?).

121 The simulations use a grid of 128 radial points, 48 in the polar angle θ and 96 in the
 122 azimuthal angle ϕ , equidistant in the radial direction. The simulation domain is confined be-
 123 tween two concentric shells around the exoplanet, with the inner boundary $R_{in} = 2R_{ex}$ (R_{ex}
 124 the exoplanet radius) and the outer boundary $R_{out} = 30R_{ex}$. The upper ionosphere model ex-
 125 tends between the inner boundary and $R = 2.5R_{ex}$.

126 The exoplanet magnetic field is rotated 90° in the YZ plane with respect to the grid poles
 127 with the aim of avoiding numerical issues (no special treatment was included for the singu-
 128 larity at the magnetic poles). The exoplanet magnetosphere is identical to the Earth magne-
 129 tosphere, thus the tilt of the Earth rotation axis is also included (23° with respect to the eclip-
 130 tic plane).

131 The simulation frame assumed is: z-axis is provided by the planetary magnetic axis point-
 132 ing to the magnetic north pole, star-planet line is located in the XZ plane with $x_{star} > 0$ (so-
 133 lar magnetic coordinates) and the y-axis completes the right handed system.

134 The response of the exoplanet magnetosphere for different SW dynamic pressure (P_d),
 135 IMF intensity ($|B|_{IMF}$) and orientation is calculated based on the data regression obtained by
 136 the set of simulations performed in ? (?) (see Table 5). The SW dynamic pressure is defined
 137 as $P_d = m_p n_{sw} v_{sw}^2 / 2$, with m_p the proton mass, n_{sw} the SW density and v_{sw} the SW veloc-
 138 ity.

139 The effect of different IMF orientations are included in the analysis: Exoplanet-star and
 140 star-exoplanet (also called radial IMF configurations), southward, northward and ecliptic clock-
 141 wise. Exoplanet-star and star-exoplanet configurations indicate an IMF parallel to the SW ve-
 142 locity vector. Southward and northward IMF orientations show an IMF perpendicular to the
 143 SW velocity vector in the XZ plane.

144 **3 Magnetopause standoff distance for exoplanets with an Earth-like magnetic field**

145 This section is dedicated to calculate the magnetopause standoff distance of exoplanets
 146 with an Earth-like magnetic field exposed to different space weather conditions. A detailed de-
 147 scription of the standoff distance calculation in the simulations is shown in the appendix. The
 148 analysis includes regular and CME-like space weather conditions expected for exoplanet or-
 149 biting inside the habitable zone of M and F stars. Consequently, the study provides a first or-
 150 der assessment of the exoplanet habitability with respect to the SW direct deposition on the
 151 exoplanet surface. The analysis is performed assuming exoplanets with an Earth-like magnetic
 152 field because no observational data exists regarding the properties of exoplanets magnetosphere.
 153 Nevertheless, the different IMF orientations tested are equivalent to exoplanets with different
 154 tilt angles.

155 The space weather conditions inside the stellar habitable zone change with the star char-
 156 acteristics (?, ?, ?, ?, ?, ?). The habitable zone for main sequence F stars ($1.1 - 1.5M_{Sun}$)
 157 is located between 2.5 - 5 au (?, ?), G stars ($1.1 - 0.9M_{Sun}$) between 0.84 - 1.68 au (?, ?), K
 158 stars ($0.9 - 0.5M_{Sun}$) between 0.21 - 1.27 au (?, ?) and M stars ($< 0.5M_{Sun}$) between 0.03
 159 - 0.25 au (?, ?). In the following, the habitability conditions imposed by the star in exoplan-
 160 ets at different orbits inside the habitable zone of M and F stars are studied.

161 The habitability conditions obtained in the simulations are defined with respect to the
 162 magnetopause standoff distance above the exoplanet surface. If the normalized standoff dis-
 163 tance is $R_{mp}/R_{ex} = 1$ (R_{mp} is the exoplanet magnetopause standoff distance) there is a direct
 164 precipitation of the SW towards the exoplanet surface. This is the same criteria used in ? (?)
 165 (equations 5 and 6).

Regular SW			
AU	n_{sw} (cm^{-3})	$ v_{sw} $ (km/s)	P_d (nPa)
0.05	2000	540	488
0.1	500	650	177
0.2	90	700	37
CME-like SW			
AU	n (10^3 cm^{-3})	$ v $ (km/s)	P_d (10^3 nPa)
0.05	40	1350	61
0.1	10	1650	23
0.2	1.8	1750	4.6

Table 1. Exoplanet orbit inside the habitable zone of M stars (first column). SW density (second column), velocity (third column) and dynamic pressure (fourth column) for regular and CME-like space weather conditions.

3.1 Exoplanet hosted by M stars

M type stars habitability conditions are an open issue because exoplanets inside the habitable zone are likely to be tidally locked (?, ?, ?) and exposed to a strong radiation from the host star (?, ?) as well as persistent CME events (?, ?, ?). Nevertheless, recent studies indicate tidal locking may constrain but not preclude the habitability conditions of exoplanets (?, ?, ?, ?). Previous studies also assessed the space weather conditions in the orbit of exoplanets inside the habitable zone of M stars (?, ?, ?, ?). Table 1 shows the density, velocity and dynamic pressure of the SW generated by a M star at different orbits following ? (?) SW model for regular and CME-like space weather conditions. The CME-like space weather conditions are guess educated values assuming 20 times the SW density and 2.5 times the SW velocity of the regular space weather conditions. Such parameters are typical for CME conditions for the Sun.

Figure 1 shows the exoplanet habitability constrain imposed by the space weather conditions inside the habitable zone of a M star. The graphs indicate the critical IMF intensity and SW dynamic pressure required for the direct SW precipitation towards the exoplanet surface in the equatorial region (for different IMF orientations), that is to say, the space weather conditions leading to a normalized exoplanet magnetopause standoff distance of $R_{mp}/R_{ex} = 1$. It should be noted that the graphs show the data regression obtained by the simulation performed in ? (?), dedicated to calculate the Earth magnetopause standoff distance for different values of the SW dynamic pressure, IMF intensities and IMF orientations. The range of SW dynamic pressure and IMF intensity values included in the study correspond to regular (panel a) and CME-like (panel b) space weather conditions. The horizontal dashed lines indicate the SW dynamic pressure at the orbit of an exoplanet at 0.05 au (red), 0.1 au (orange) and 0.2 au (blue) from the host star based on ? (?) SW model, providing a reference value of the critical IMF intensity required for the direct SW precipitation onto the exoplanet surface for different IMF orientations based on the pressure balance (see appendix).

During regular space weather conditions, panel a, the critical IMF intensity for an exoplanet at 0.2 au is $|B|_{IMF} > 5000 \text{ nT}$, $\approx 2050 \text{ nT}$ at 0.1 au and $\approx 1100 \text{ nT}$ at 0.05 au if the IMF is southward. The southward IMF is highlighted along the article because it is the IMF orientation leading to the lowest magnetopause standoff distance (maximum reconnection) for a fixed IMF intensity. Consequently, the magnetic field generated by M stars must be very large to threaten the exoplanet habitability. Nevertheless, the magnetic field of young

AU	P_{rot} (days)	n_{sw} (cm^{-3})	$ v_{sw} $ (km/s)	P_d (nPa)	$ B _{IMF}$ (10^3 nT)
0.05	24	4500	280	295	2.16
0.05	12	4500	360	488	17.7
0.05	6	4500	400	602	25.9
0.05	3	4500	450	762	30.3
0.1	24	900	350	92.2	0.54
0.1	12	900	440	146	4.43
0.1	6	900	510	196	6.46
0.1	3	900	620	289	7.57
0.2	24	240	410	33.7	0.31
0.2	12	240	500	50.2	1.11
0.2	6	240	590	69.9	1.62
0.2	3	240	800	128	1.89

Table 2. Exoplanet orbit inside the habitable zone of M stars (first column). Star rotation period (second column). SW density (third column), velocity (fourth column) and dynamic pressure (fifth column). IMF intensity (sixth column).

198 and fast rotating M stars can overcome such IMF intensity thresholds (?, ?, ?) reaching val-
199 ues up to 4 kG. The IMF intensity threshold during a CME largely decreases compared to reg-
200 ular space weather conditions, panel b. If the exoplanet orbit is at 0.2 au, the critical $|B|_{IMF} \approx$
201 310 nT for a southward IMF and ≈ 1100 nT for a star-exoplanet IMF. If the exoplanet is at
202 0.1 au, $|B|_{IMF} \approx 110$ nT for a southward IMF, ≈ 500 nT for a star-exoplanet IMF and ≈ 3750
203 nT for a northward IMF. If the exoplanet is at 0.05 au, $|B|_{IMF} \approx 60$ nT for a southward IMF,
204 ≈ 325 nT for a star-exoplanet IMF and ≈ 2100 nT for a northward IMF. That is to say, ex-
205 oplanets at 0.2 au are efficiently protected during CME space weather conditions if the inten-
206 sity of the magnetic field generated by the M star is not strong enough to exceed 310 nT. On
207 the other hand, exoplanets at ≤ 0.1 au are exposed to the direct SW precipitation during CMEs
208 if the IMF intensity exceeds 110 nT. In summary, exoplanets at 0.2 au should be protected from
209 the direct precipitation of the SW by an Earth-like magnetic field, thus the exoplanets is hab-
210 itable with respect to the SW shielding. It should be noted that present study conclusions are
211 consistent with respect to configuration subsets analyzed by other authors (?, ?, ?).

212 As it was mentioned in the previous paragraph, the space weather conditions change with
213 the rotation rate of the star, because the magnetic activity and the properties of the SW gen-
214 erated by the star change (?, ?). The SW velocity during regular space weather conditions is
215 2 times larger if the star rotation is 4 times faster, although the SW density and temperature
216 is weakly affected (?, ?). In addition, faster rotators have a stronger magnetic activity, because
217 the large-scale surface magnetic field ($B_{surf,*}$) dependency with the Rossby number (R_o) is $B_{surf,*} \propto$
218 $R_o^{-1.3}$ (?, ?, ?). Thus the IMF intensity at the exoplanet orbit is higher as well as the CME fre-
219 quency and intensity (?, ?, ?). Consequently, if the effect of the M star rotation period is in-
220 cluded in the analysis, the threshold of the IMF intensity and SW dynamic pressure for the
221 direct precipitation of the SW toward the exoplanet surface changes. Table 2 indicates the SW
222 density and velocity in the orbit of an exoplanet at 0.05, 0.1 and 0.2 au from the host M star
223 for different rotation periods (P_{rot}) for the star during regular space weather conditions (data
224 derived from ? (?) simulations). The SW density has a weak dependency with the star rota-
225 tion but the SW velocity and IMF intensity increases with the star rotation. The range of M
226 star rotation periods analyzed include the majority of the 795 M stars identified by Kepler mis-
227 sion as a sub-sample of the 12000 main sequence stars identified (?, ?). Nevertheless, recent
228 surveys of M star identified an important population of slow M stars rotators, showing rota-
229 tion periods between 30 to 120 days (?, ?, ?).

Figure 2 indicates the IMF intensity and SW dynamic pressure threshold with respect to the M star rotation rate for regular space weather conditions.

The model shows a large decrease of the IMF intensity threshold if the M star rotation period decreases given a SW dynamic pressure. $\Delta|B|_{IMF}$ is indicated by the bold arrows in the top of the graph for each IMF orientation between the cases of star with rotation rates of 24 and 3 days. For an exoplanet at 0.05 au, the IMF intensity threshold decreases from 1500 nT to 850 nT reducing the star rotation period from 24 to 3 days if the IMF is southward, as well as from 3000 nT to 2000 nT if the IMF is in the exoplanet-star orientation. Regarding an exoplanet orbit at 0.1 au, the IMF intensity threshold decreases from 3250 nT to 1500 nT for a southward IMF, as well as from 4750 nT to 3000 nT for an exoplanet-star IMF. If the exoplanet orbit is located at 0.2 au, the IMF intensity threshold decreases from 5550 nT to 2600 nT for a southward IMF and from 7000 nT to 4250 nT for an exoplanet-star IMF. The IMF intensity threshold obtained can be compared with the magnetic field generated by M stars at different orbits following ? (?) simulations (last column of table 2). At 0.05 au, the IMF intensity is above the threshold for a Southward IMF orientation if the star rotation period is shorter than 24 days, and below the threshold for an exoplanet-star IMF if the rotation period is 24 days or larger. That is to say, favorable habitability conditions with respect to SW of an exoplanet at 0.05 au require an intrinsic magnetic field stronger than Earth's if the rotation rate of the M star is 24 days or smaller. At 0.1 au, the IMF intensity is above the threshold for Southward and exoplanet-star IMF orientation and the rotation rate is 12 days or faster. Thus, exoplanets at 0.1 au require a magnetic field stronger than the Earth if the host M star rotation rate is smaller than 12 days. If the exoplanet is at 0.2 au, the IMF intensity is below the threshold for all IMF orientations if the star rotation rate is 3 days or slower, so an Earth-like magnetic field can efficiently shield the exoplanet surface.

Summarizing, exoplanets with an Earth-like magnetic field hosted by a M star and located at 0.2 au are shielded from the SW during regular and CME-like space weather conditions. In addition, such protection holds for M stars with rotation periods as fast as 3 days during regular SW space weather conditions. Nevertheless, fast rotating M stars with strong and recurrent CME-like events can restrict the exoplanet habitability conditions. On the other hand, exoplanets at 0.1 au are shielded from regular and CME-like space weather conditions only if the M stars rotation period is 12 days or larger. Finally, exoplanets at 0.05 au are vulnerable during CME-like events even for M stars with the a rotation period of 24 days, thus exoplanet habitability requires a magnetic field stronger with respect to the Earth. Nevertheless, exoplanet at 0.05 au hosted by slower rotators with $P_{rot} > 24$ days are protected during standard and CME-like events by an Earth-like magnetic field if the IMF intensity is lower than 1000 nT for a southward IMF.

3.2 Exoplanet hosted by F stars type τ Boo

Space weather conditions in F stars were analyzed in previous studies, particularly for τ Boo type *F7V*, concluding the SW may have a density 135 times larger with respect to the SW generated by the Sun, as well as a velocity around 300 km/s (?). Table3 shows guess educated values of the space weather conditions in the orbit of an exoplanet hosted by a F star similar to τ Boo near the bottom and upper range of the habitable zone. The SW density during regular space weather conditions is assumed 100 times the SW density generated by the Sun at 2.5 and 5 au. The velocity is the same with respect to (?), 300 km/s at 2.5 au. In addition, an extrapolation is assumed to characterize the space weather conditions during CMEs, selecting a SW density 20 times larger and a velocity 5 times higher with respect to the regular space weather conditions.

Figure 3 indicates the critical IMF intensity and SW dynamic pressure required for the direct SW precipitation towards an exoplanet hosted by a F star type τ Boo inside the habitable zone during CME-like space weather conditions. The same analysis for regular space weather conditions is not included because the IMF intensity and SW dynamic pressure are

Regular SW			
AU	n_{sw} (cm^{-3})	$ v_{sw} $ (km/s)	P_d (nPa)
2.5	50	300	3.8
5.0	20	310	1.6
CME-like SW			
AU	n (10^3 cm^{-3})	$ v_{sw} $ (10^3 km/s)	P_d (10^3 nPa)
2.5	1.0	1.5	1.88
5.0	0.4	1.55	0.8

Table 3. Exoplanet orbit inside the habitable zone of F star type τ Boo (first column). SW density (second column), velocity (third column) and dynamic pressure (fourth column) for regular and CME-like space weather conditions.

281 well below the threshold required for the direct SW precipitation, that is to say, the exoplanets
282 at 2.5 – 5.0 au are shielded during regular space weather conditions.

283 Exoplanets located at 5 au show an IMF intensity threshold of $|B|_{IMF} \approx 825$ nT for a
284 southward IMF and $|B|_{IMF} \approx 2300$ nT for an exoplanet-star IMF. Regarding exoplanets at
285 2.5 au, the IMF intensity threshold is $|B|_{IMF} \approx 500$ nT for a southward IMF and $|B|_{IMF} \approx$
286 1550 nT for an exoplanet-star IMF. It must be noted the magnetic activity of τ Boo is larger
287 with respect to the Sun, showing a shorter magnetic cycle of 2 years (?, ?, ?). It is known that
288 F stars have a slower decrease of the rotation rate along the main sequence, leading to a stronger
289 magnetic field compared to G stars (?, ?, ?) with the exception of low mass stars populations
290 ($< 0.9M_{Sun}$) that maintain rapid rotation for much longer than solar-mass stars (?, ?). Con-
291 sequently, the effect of the CME on exoplanets orbiting inside the habitable zone of F star, par-
292 ticular τ Boo, can increase the exoplanet habitability conditions if the frequency of these ex-
293 treme space weather events is high.

294 Next step of the analysis is to include the effect of stellar rotation. The F star rotation
295 period is lower with respect to less massive stars such as G, K and M stars. The lower bound
296 is around 2 days for $F0$ stars increasing to 10 days for $F9$ stars (?, ?). Table 4 indicates guess
297 educated values of the SW dynamic pressure and IMF intensity at different exoplanet orbits
298 for different F star rotation periods during CME space weather conditions. The values of the
299 IMF intensity are extrapolated from observational data of F stars magnetic field magnitude (?,
300 ?, ?, ?, ?) and modeling results (?, ?). We assume the SW velocity increases with the star
301 rotation although the SW density and temperature is constant, extrapolating ? (?) results.

302 Figure 4 indicates the IMF intensity and SW dynamic pressure threshold with respect
303 to the F star rotation rate for CME-like space weather conditions.

304 The simulations indicate the habitability of exoplanets at 2.5 au from the host F star is
305 conditioned by the SW if the star rotation period is shorter than 10 days. The exoplanet sur-
306 face is protected if the star rotation period is 10 days or above, showing an IMF intensity of
307 500 nT that is smaller compared to the IMF intensity required for the direct SW precipitation
308 . For a stellar rotation of 7.5 or 5 days, direct SW precipitation exists during a southward IMF
309 with 675 and 575 nT, respectively, smaller than the IMF intensity during CMEs. The IMF thresh-
310 old for the direct SW precipitation is also largely exceeded if the star rotation is 2 days for
311 an IMF oriented in the Southward or Exoplanet-star directions. Consequently, exoplanets at
312 2.5 au requires an intrinsic magnetic field intensity stronger with respect to the Earth if the

AU	P_{rot} (days)	n_{sw} (10^3 cm^{-3})	$ v_{sw} $ (10^3 km/s)	P_d (10^3 nPa)	$ B _{IMF}$ (10^3 nT)
2.5	2	1.0	1.7	2.4	3
2.5	5	1.0	1.3	1.4	1.5
2.5	7.5	1.0	1.15	1.1	1
2.5	10	1.0	1.0	0.8	0.5
5.0	2	0.4	1.75	1.0	0.75
5.0	5	0.4	1.35	0.6	0.4
5.0	7.5	0.4	1.2	0.5	0.25
5.0	10	0.4	1.05	0.4	0.1

Table 4. Exoplanet orbit inside the habitable zone of F star (first column). Star rotation period (second column). SW density (third column), velocity (forth column) and dynamic pressure (fifth column). IMF intensity (sixth column).

313 star rotation period is smaller than 10 days. On the other hand, the simulations show that ex-
 314 oplanets with orbits at 5.0 au are protected during CME-like space weather conditions if the
 315 star rotation period is above 2 days. In the case of the rotation period is 2 days the IMF in-
 316 tensity threshold is similar to the IMF intensity during CMEs (around 25 nT smaller).

317 In summary, regular space weather conditions does not impact the habitability of exo-
 318 planets in the habitable zone of F stars type τ Boo. On the other hand, persistent and strong
 319 CME events can largely influence the habitability of exoplanets nearby the inner boundary of
 320 the habitable zone, thus a stronger magnetic field regarding the Earth magnetic field is manda-
 321 tory. Nevertheless, exoplanets at the outer region of the habitable zone could be efficiently shielded
 322 by an Earth-like magnetic field. The analysis of the star rotation effect on the habitability state
 323 due to the SW indicates that exoplanets with an Earth-like magnetic field at 5.0 au are effi-
 324 ciently protected during extreme space weather conditions if the star rotation period is larger
 325 than 2 days. On the other hand, exoplanets at 2.5 au requires an intrinsic magnetic field stronger
 326 regarding the Earth if the star rotation period is smaller than 10 days. It should be noted that
 327 the rotation period of τ Boo is 3.3 days, thus habitability conditions due to the space weather
 328 require an exoplanet magnetic field stronger compared to the Earth. That means, habitability
 329 conditions may relax for the case of F stars in the spectral range from $F7$ to $F9$ because the
 330 rotation period is larger (10 days or higher) (?). Nevertheless, the habitable zone of $F7$ to
 331 $F9$ stars displaces closer to the star, located between 1.1 to 2.5 au. Consequently, exoplanets
 332 located in the outer region of the habitable zone of $F7$ to $F9$ stars require, at least, a magnetic
 333 field similar to the Earth to avoid the direct SW precipitation during CMEs, although it must
 334 be stronger if the orbit is closer to the star or the star rotation period is shorter than 10 days.

335 4 Radio emission from exoplanets with an Earth-like magnetosphere

336 Radio emission from exoplanet magnetospheres and space weather conditions are closely
 337 connected. Radio emission measurements may provide information of the exoplanet magnetic
 338 field and, once the characteristics of the exoplanet magnetic field are inferred, insights about
 339 the space weather conditions generated by the host star on the exoplanet orbit. This section
 340 is dedicated to the analysis of the influence of the space weather conditions, from regular to
 341 CME-like, on the radio emission generation, providing simplified new tools for the interpre-
 342 tation of radio telescopes observational data.

343 The interaction of the SW with a planetary magnetosphere can be analyzed using the
 344 analogous of a flow facing a magnetized object, leading to the partial transfer of the flow en-
 345 ergy. The transferred energy is transformed to radiation and the radiation power (P_{disp}) is pro-
 346 portional to the intercepted flux of the magnetic energy. Thus, following the radio-magnetic

347 Bode's law, the incident magnetized flow power and the obstacle magnetic field intensity can
 348 be used to approximate the radio emission as $P_w = \beta[P_{disp}]^n$, with P_w the radio emission power,
 349 β the efficiency of dissipated power to radio emission conversion with $n \approx 1$ (? , ? , ?) and $\beta \approx$
 350 $2 \cdot 10^{-3} - 10^{-2}$ (? , ?).

The power dissipated in the interaction between the SW with the magnetosphere is calculated at the exoplanet day side. Irreversible processes in the interaction convert internal, bulk flow kinetic and magnetic energy into the kinetic energy required to accelerate the electrons along the magnetic field lines, and leading to cyclotron-maser radiation emission by these accelerated electrons. The energy transfer can be evaluated analyzing the energy fluxes of the system. There is a detailed discussion of the flux balance in ? (?). The radio emission is calculated using the net magnetic power deposited on the exoplanet day side (? , ? , ? , ?):

$$P_w = 2 \cdot 10^{-3} P_B = 2 \cdot 10^{-3} \int_V \vec{\nabla} \cdot \frac{(\vec{v} \wedge \vec{B}) \wedge \vec{B}}{\mu_0} dV$$

351 with P_B the divergence of the magnetic Poynting flux associated with the hot spots of energy
 352 transfer in the exoplanet day side and V the volume enclosed between the bow shock nose and
 353 the magnetopause.

354 In the following, the radio emission is calculated during regular and CME-like space weather
 355 conditions, modifying the SW dynamic pressure as well as IMF intensity and orientation of
 356 the model. First, the effect of the SW dynamic pressure and IMF intensity on the radio emission
 357 is analyzed separately. Next, the trends of the radio emission with respect to the SW dynamic
 358 pressure and IMF intensity are evaluated together.

359 4.1 Effect of the SW dynamic pressure

360 This section is dedicated to the study of the exoplanet radio emission generation with
 361 respect to the SW density and velocity, hence the SW dynamic pressure. Particular emphasis
 362 is dedicated to clarify the link between bow shock compression and radio emission generation.
 363

364 Figure 5 shows the logarithm of the radio emission power at the exoplanet day side for
 365 a set of SW dynamic pressure values increasing the SW velocity (fixed the SW density to 12
 366 cm^{-3} , panel a) and increasing the SW density (fixed the SW velocity to 350 km/s, panel b)
 367 for a star-exoplanet IMF orientation with $|B|_{IMF} = 10$ nT. Simulations with $P_d < 10$ nPa
 368 are analyzed separately due to the effect of the magnetosphere thermal pressure on the mag-
 369 netopause standoff distance, negligible in the simulations with $P_d \geq 10$ nPa (? , ?).

370 The radio emission increases from 10^6 to 10^{10} W as the SW increases from regular to
 371 super CME-like space weather conditions. The order of magnitude of the radio emission power
 372 calculated in the simulations is consistent with ? (?) scaling (around $6 \cdot 10^7$ W) for SW ve-
 373 locity values between $500 - 1200$ km/s ($P_d = 2.5 - 14$ nPa) and SW density values between
 374 $30 - 120$ cm^{-3} ($P_d = 3.1 - 13.3$ nPa), that is to say, the radio emission values obtained from
 375 the simulations and the scaling are similar for regular space weather conditions. If $P_d < 2.5$
 376 nPa, the radio emission power is below 10^7 W. For common CME-like conditions ($15 < P_d <$
 377 40 nPa) the radio emission power increases up to $6 \cdot 10^8$ W. During strong CME-like space
 378 weather conditions ($40 < P_d < 100$ nPa) the radio emission power reaches 10^9 W. For su-
 379 per CME-like space weather conditions ($P_d > 100$ nPa) the radio emission power is $2 \cdot 10^9$
 380 W. The enhancement of the radio emission as P_d increases is caused by a higher net magnetic
 381 power dissipation at the exoplanet day side as the magnetosphere compression intensifies.

382 Next, the trends of the radio emission with respect to the SW density and velocity are
 383 analyzed. Figure 6, panels a and c, show the fit of the radio emission power to the square value
 384 of the SW velocity $P_w \propto \Gamma(v_{sw}^2)^\alpha$ if $P_d \leq 10$ nPa and > 10 nPa, respectively. Figure 6, pan-
 385 els b and d, show the fit of the radio emission power to the SW density $P_w \propto \Gamma(n_{sw})^\alpha$ if $P_d \leq$
 386 10 nPa and > 10 nPa, respectively. The radio emission trends are analyzed separately in the

$P_d \leq 10$ (nPa)		
Regression	Γ	α
Velocity	$(2 \pm 3) \cdot 10^5$	1.2 ± 0.1
Density	$(2 \pm 1) \cdot 10^5$	1.3 ± 0.2
$P_d > 10$ (nPa)		
Velocity	$(3 \pm 4) \cdot 10^{-4}$	1.84 ± 0.08
Density	$(1.2 \pm 0.3) \cdot 10^4$	1.82 ± 0.04

Table 5. Regression parameters in simulations with different SW velocity and density values. (a) Variable SW parameter in the data regression, (b) Γ factor and (c) α exponent. Trends in the simulations with $P_d \leq 10$ nPa and $P_d > 10$ nPa are analyzed separately.

387 simulations with $P_d \leq 10$ nPa and > 10 nPa to isolate the effect of the thermal pressure caused
 388 by the magnetosphere (for more information please see ? (?)). The parameters of the data re-
 389 gression are indicated in table 5.

The data fit finds similar exponents for the regression $P_w \propto (v_{sw}^2)^\alpha$ and $P_w \propto (n_{sw})^\alpha$ if $P_d \leq 10$ nPa, that is to say, proportional to the SW dynamic pressure. The scaling of the radio emission with respect to the SW dynamic pressure is stronger in simulations with $P_d > 10$ nPa, thus the radio emission generation is further promoted in a compressed magnetosphere. This is explained by the enhancement of the Poynting flux divergence as the magnetopause is located closer to the exoplanet surface. The regression parameters can be compared with the theoretical expression of the radio emission induced by a magnetized flow dominated by the dynamic pressure facing a magnetized obstacle (?, ?, ?):

$$P_W = \beta \frac{|B_{IMF,\perp}|^2 B_{ex}^{2/3}}{\mu_0^{4/3}} \left(\frac{v_{sw}}{m_p n_{sw}} \right)^{1/3} R_{ex}^2 \pi \frac{2.835}{K^{1/3}}$$

390 with $B_{IMF,\perp}$ the perpendicular component of the IMF with respect to the flow velocity, B_{ex} the
 391 intensity of the magnetic field in the equator of the magnetized obstacle, μ_0 the vacuum mag-
 392 netic permeability and $K = 1-2$. Here, the intercepted flux of magnetic energy is estimated
 393 as $P_{disp} = \epsilon (v_{sw} |B_{IMF,\perp}|^2 / \mu_0) \pi R_{obs}^2$ with $\epsilon = M_A / (1 + M_A^2)^{1/2}$ (M_A Alfvénic Mach number),
 394 $R_{obs} = 1.5 R_{mp}$ and $R_{mp} = R_{ex} (2 B_{ex} / (\mu_0 K n_{sw} v_{sw}^2))^{1/6}$. Thus, the theoretical dependency of
 395 the radio emission power with the SW velocity is $v_{sw}^{0.33}$ and with the SW density is $n_{sw}^{-0.33}$. The
 396 radio emission calculated in the simulations (all dominated by the SW dynamic pressure be-
 397 cause $P_{IMF} = 0.09$ nPa) shows a stronger dependency with the SW velocity compared to the
 398 theoretical model. Regarding the SW density, the simulations show a direct proportionality with
 399 the radio emission, not an inverse proportionality as the theoretical expression predicts. This
 400 discrepancy can be explained by the enhancement of the magnetosphere compression and bow
 401 shock distortion as the SW dynamic pressure increases, that is to say, the theoretical expres-
 402 sion cannot reproduce the effect of the bow shock compression associated with a modifica-
 403 tion of the energy fluxes, net magnetic power dissipated and divergence of the magnetic Poynt-
 404 ing flux in the magnetosphere day side. Thus, the theoretical scaling law could underestimate
 405 the radio emission power generated in exoplanets for space weather conditions leading to a
 406 strongly compressed bow shock.

407 The effect of the SW dynamic pressure on the radio emission generation is highlighted
 408 in figure 7, comparing the divergence of the Poynting flux in the bow shock and magnetopause
 409 region for simulations with $v_{sw} = 300$ km/s ($P_d = 0.9$ nPa) and $v_{sw} = 3000$ km/s ($P_d = 90$
 410 nPa). The Poynting flux divergence is more than one order of magnitude higher in the sim-
 411 ulation with $P_d = 90$ nPa, explaining the radio emission enhancement as the SW dynamic
 412 pressure increases. It should be noted that the maxima of the Poynting flux divergence is lo-

413 cated closer to the exoplanet surface as P_d increases because the magnetosphere standoff dis-
 414 tance is smaller. In addition, the local maxima of the Poynting flux divergence is displaced
 415 towards the South of the magnetosphere in both simulations, determined by the IMF orien-
 416 tation and in particular by the location of the reconnection region. From the observational point
 417 of view, radio telescopes may measure a signal with a more localized radio emission maxima
 418 as the bow shock compression enhances, although the radio emission maxima should be more
 419 diffused as the bow shock compression is weakened.

420 **4.2 Effect of the IMF intensity and orientation**

421 In this subsection we analyze the effect of the IMF intensity and orientation on the ex-
 422 oplanet radio emission generation. In particular, the role of the reconnection between the IMF
 423 and the exoplanet magnetic field is explored, as well as the bow shock formation or disper-
 424 sion as the SW dynamic pressure or the IMF magnetic pressure dominate, respectively.

425 The IMF can induce large distortions in the exoplanet magnetic field, modifying locally
 426 the topology of the magnetosphere, particularly in the reconnection regions between the ex-
 427 oplanet magnetic field and the IMF. Figure 8 shows the logarithm of the radio emission fixed
 428 $P_d = 1.2$ nPa for different IMF orientations (exoplanet-star, northward, southward and eclip-
 429 tic) and IMF intensities between 10 and 250 nT.

430 The same order of magnitude is obtained for the radio emission power comparing sim-
 431 ulation results and ? (?) scaling if the IMF intensity is between 20 - 125 nT for an exoplanet-
 432 star IMF, 10 - 125 nT for a northward IMF, 10 - 50 nT for a southward IMF and 10 - 70 nT
 433 for an ecliptic IMF. Consequently, the radio emission calculated in the simulations and the val-
 434 ues predicted by the scaling are similar from regular to strong CME-like space weather con-
 435 ditions regarding the IMF intensity. The simulations also predict a radio emission power above
 436 10^8 W during Super CME. The IMF orientation leading to the largest radio emission is the
 437 southward IMF, followed by the ecliptic and exoplanet-star IMF. The lowest radio emission
 438 is observed for the northward IMF. The variation of the radio emission values regarding the
 439 IMF orientation is explained by the location and intensity of the reconnection regions. The south-
 440 ward IMF orientation induces the strongest reconnection, located in the equatorial region of
 441 the magnetosphere leading to the smallest magnetopause standoff distance and the largest ra-
 442 dio emission. Likewise, the northward IMF orientation causes the lowest radio emission be-
 443 cause the reconnection region is located nearby the exoplanet poles and the magnetopause stand-
 444 off distance is larger regarding the other IMF orientations. It should be noted that the loca-
 445 tion of the radio emission maxima and the reconnection regions are concomitant in the sim-
 446 ulation, thus the radio emission maxima displaces with the reconnection region as the IMF in-
 447 tensity increases; towards the equatorial region for a southward IMF, the poles for a northward
 448 IMF, to the South of the magnetosphere for a star-exoplanet IMF, to the North for a exoplanet-
 449 star and tilted to a higher longitude for a IMF oriented in the equatorial plane.

450 Figure 9 shows the Poynting flux divergence in the bow shock and magnetopause region
 451 for simulations with an exoplanet-star IMF with $|B|_{IMF} = 30$ nT (panel a) and 250 nT (panel
 452 b). The radio emission is more than one order of magnitude larger in the simulation with $|B|_{IMF} =$
 453 250 nT.

454 The effect of the IMF orientation on the radio emission is larger in simulations with $|B|_{IMF} \geq$
 455 70 nT. On the other hand, simulations with $|B|_{IMF} < 70$ nT show similar radio emission val-
 456 ues for all the IMF orientations. This is explained by the absence of the bow shock in the sim-
 457 ulations with $|B|_{IMF} \geq 70$ nT, because the Alfvénic Mach number $M_A = v_{sw}/v_A < 1$ (v_A is
 458 the Alfvén speed). Simulations with $|B|_{IMF} < 70$ nT ($M_A > 1$) lead to the formation of the
 459 bow shock, showing two regions with a local maxima of the Poynting flux divergence: 1) the
 460 reconnection region between the IMF and the exoplanet magnetic field, 2) the nose of the bow
 461 shock where the IMF lines are compressed and bent. Figure 10 shows the radio emission from
 462 the bow shock nose, panel a, and the reconnection regions, panel b, for a simulation with south-
 463 ward IMF and $|B|_{IMF} = 30$ nT. The compression and bending of the IMF lines lead to a lo-

$M_A > 1$		
IMF	Γ	α
Southward	$(7 \pm 6) \cdot 10^5$	1.0 ± 0.3
Northward	$(2.1 \pm 0.9) \cdot 10^6$	0.74 ± 0.12
Exo-star	$(1.6 \pm 0.6) \cdot 10^6$	0.98 ± 0.14
Ecliptic	$(3 \pm 1) \cdot 10^5$	1.29 ± 0.12
$M_A < 1$		
Southward	$(5 \pm 9) \cdot 10^3$	2.0 ± 0.3
Northward	$(1.0 \pm 0.6) \cdot 10^5$	1.94 ± 0.11
Exo-star	$(3 \pm 3) \cdot 10^2$	2.8 ± 0.12
Ecliptic	$(2 \pm 2) \cdot 10$	3.3 ± 0.2

Table 6. Regression parameters in simulations with different IMF orientations and intensities. IMF orientation (first column), Γ factor (second column) and α exponent (third column). The trends in simulations with $M_A > 1$ and $M_A < 1$ are analyzed separately.

464 cal maxima of the Poynting flux divergence in the nose of the bow shock. On the other hand,
 465 the Poynting flux divergence is larger and more localized in the magnetopause region where
 466 the IMF and the exoplanet magnetic field reconnects, closer to the exoplanet surface. Conse-
 467 quently, if the bow shock exists, the Poynting flux divergence in the bow shock depends on
 468 the SW dynamic pressure as well, thus the role of the IMF orientation in the radio emission
 469 generation is smaller. Radio telescopes may measure a signal with well defined radio emis-
 470 sion maxima if the bow shock does not exist, although showing a fast variability of the max-
 471 ima location as the IMF orientation changes.

Figure 11 and table 6 show the fit of the radio emission values calculated in the sim-
 ulations using the regression $P_w \propto \Gamma |B|_{IMF}^\alpha$. It should be noted that the IMF pressure in the
 simulations with $|B| > 50$ nT is larger than the SW pressure ($P_{IMF} > 1.2$ nPa). In such con-
 figurations the theoretical expression of the radio emission is (?, ?, ?):

$$P_W = \beta \frac{v_{sw} |B_{IMF,\perp}|^{4/3}}{\mu_0} R_{ex}^2 B_{ex}^{2/3} 3.6\pi$$

472 Here, $R_{mp} = R_{ex} (2B_{ex}/|B_{IMF,\perp}|)^{1/3}$. Thus, the theoretical dependency of the radio emission
 473 power with the SW velocity is linear with the v_{sw} and a super linear with the intensity of an
 474 IMF perpendicular to the plasma flow. Consequently, the scaling for the simulations with dom-
 475 inant dynamic pressure or dominant IMF pressure must be analyzed separately.

476 The regression exponents indicate the radio emission dependency with the IMF inten-
 477 sity is weaker in simulations with dominant SW pressure compared to simulations with dom-
 478 inant IMF pressure. This is the opposite tendency with respect to the radio-magnetic scaling
 479 law that predicts a stronger $|B|_{IMF}$ trend if the SW pressure is dominant ($|B_{IMF,\perp}|^2$). This in-
 480 consistency can be explained by the effect of the bow shock compression in the simulations.
 481 On the other hand, the regression exponents obtained in simulations with dominant IMF pres-
 482 sure and Southward / Northward IMF orientations are similar to the radio-magnetic scaling
 483 law if the dynamic pressure is dominant ($\alpha \approx 2$). That is to say, radio-magnetic scaling law
 484 and simulation lead to similar trends if the bow shock does not exist and the IMF is perpen-
 485 dicular to the SW velocity. Consequently, deviations appear if the IMF is unaligned with the
 486 exoplanet magnetic field axis and the role of bow shock compression is added in the analy-
 487 sis, effects not included in the radio-magnetic scaling law. In summary, the theoretical scal-
 488 ing law could underestimate the radio emission power generated in exoplanets during space
 489 weather conditions leading to the bow shock dispersion.

IMF	Z	M	N
Southward	5.45 ± 0.15	1.22 ± 0.07	0.95 ± 0.03
Northward	5.68 ± 0.17	1.09 ± 0.08	0.97 ± 0.03
Exoplanet-star	5.8 ± 0.3	0.90 ± 0.12	1.15 ± 0.05
Ecliptic	5.7 ± 0.2	1.13 ± 0.07	0.99 ± 0.03

Table 7. Regression parameters in simulations with different SW dynamic pressure, IMF orientation and intensity. IMF orientation (first column), Z parameter (second column), M parameter (third column) and N parameter (fourth column).

4.3 Combined effect of the SW dynamic pressure, IMF intensity and IMF orientation

The analysis of the combined effect of SW dynamic pressure, IMF intensity and orientation provides an improved approach of the radio emission generation trends, particularly during extreme space weather conditions that melds a large compression of the bow shock and an intense magnetic reconnection.

Figure 12 shows the logarithm of the radio emission with respect to the SW dynamic pressure, IMF intensity and orientation for CME-like space weather conditions ($P_d = 1.5 - 100$ nPa and $|B|_{IMF} = 50 - 250$ nT). It should be noted that the increment of the SW dynamic pressure in the simulations is done by increasing the velocity of the SW, thus the SW density is fixed in the simulations. The radio emission ranges from $3 \cdot 10^8$ W for common CME (20 nPa and 50 nT) to above 10^{10} W for super CME-like space weather conditions (100 nPa and 250 nT). A large bow shock compression (large SW dynamic pressure) combined with a strong reconnection between IMF and exoplanet magnetic field (IMF intensity is high) lead to a further enhancement of the radio emission. The simulations with large SW dynamic pressure show similar radio emission values independently of the IMF intensity and orientation. On the other hand, the radio emission show larger changes between simulations with different IMF intensity and orientation if the SW dynamic pressure is low. Again, this result is consistent with previous analysis because simulations with low SW dynamic pressure and large IMF (particularly if $M_A < 1$) show a larger effect of the IMF intensity and orientation on the radio emission.

Figure 13 and table 7 indicate the data fit and the parameters of the regression $\log P_W \propto \log Z + M \log(|B|_{IMF}) + N \log(P_d)$, respectively. This expression is derived from $P_W \propto Z |B|_{IMF}^M P_d^N$. The data regression includes simulations with dominant SW and dominant IMF pressure because the main part of the space weather conditions analyzed have a dominant SW pressure, indicated by the black dashed line in figure 12 (SW dominant cases above the line).

The regression parameters with respect to the IMF intensity show similar trends compared to simulations with fixed SW dynamic pressure if the bow shock exist ($M \approx 1$ and $\alpha \approx 1$, see table 6 and 7). On the other hand, the scaling with respect to the SW dynamic pressure is weaker compared to simulations with fixed IMF intensity and orientation ($N \approx 1$ although $\alpha \approx 1.8$ if $P_d > 10$ nPa, see table 5 and 7). Consequently, the simulations analysis indicate the effect of the IMF intensity on the radio emission is similar to the SW dynamic pressure if the bow shock exist and it is strongly compressed. In addition, there is a variation of the radio emission scaling with respect to the IMF orientation up to 20%, pointing out the important role of the IMF orientation on the radio emission generation. If the exponents of the data regression are compared to the radio-magnetic scaling law for a dominant SW dynamic pressure, there is clear deviation showing a weaker trend for $|B|_{IMF}$ ($M \approx 1$ versus 2) although stronger for P_d ($N \approx 1$ versus 0.17). Such difference is smaller if the regression exponents are compared to the radio-magnetic scaling law for a dominant IMF pressure, showing a similar $|B|_{IMF}$ exponent ($M \approx 1$ versus 1.33) and a P_d exponent 2 times larger ($N \approx$

1 versus 0.5). Indeed, the best agreement is obtained if the IMF orientation is Southward ($M =$
 1.22 and $N = 0.95$). Consequently, as it was previously discussed, the discrepancy with the
 radio-magnetic scaling law for the configurations with dominant SW pressure could be caused
 by the effect of the bow shock compression.

4.4 Analysis result consequences on the interpretation of radio telescope measurements

The analysis of the radio emission generated in exoplanet magnetospheres for different
 space weather conditions provides useful information regarding the variability of the radio emis-
 sion signal measured by radio telescopes. In addition, an order of magnitude approximation
 of the radio emission generated by exoplanets with an Earth-like magnetosphere is provided
 for different space weather conditions.

The combined effect of a strongly compressed bow shock and an intense reconnection
 between the IMF and the exoplanet magnetic field can lead to a large increase of the radio emis-
 sion generation. For the case of an exoplanet with an Earth-like magnetic field, the radio emis-
 sion can increase more than four orders of magnitude comparing regular and extreme space
 weather conditions (super CME-like events for the case of the Earth).

The simulations indicate that the largest radio emission variability should be observed
 from exoplanets hosted by stars with large magnetic activity and low SW dynamic pressure,
 leading to space weather conditions that avoid the formation of the bow shock. The radio emis-
 sion variation for a given SW dynamic pressure could be close to one order of magnitude re-
 garding the IMF orientation. On the other hand, if the exoplanet is hosted by stars with low
 magnetic activity although large SW dynamic pressure, the variability of the radio emission
 with the IMF orientation should be small and mainly induced by changes on the SW dynamic
 pressure. The variation of the radio emission with the IMF in simulations with bow shock is
 smaller than a factor 1.5.

The study also shows that, if the host star generates a SW with large dynamic pressure
 and an intense IMF, the effect of the IMF orientation should also induce an substantial vari-
 ability on the radio emission signal even if the bow shock exist, close to a factor 2. Conse-
 quently, a large radio emission variability is linked to unfavorable space weather conditions
 because the host star magnetic activity is large, leading to a strong reconnection between IMF
 and exoplanet magnetic field, reducing the magnetopause standoff distance. The same way,
 a strong radio emission signal combined with a small variability indicates a compressed mag-
 netosphere, that is to say, the SW dynamic pressure generated by the host star is large also
 reducing the magnetosphere standoff distance.

The simulations scaling shows an underestimation of the exoplanet radio emission by
 the theoretical scaling for space weather conditions leading to a strongly compressed or van-
 ishing bow shock. Consequently, the radio telescope sensibility required to measure the ra-
 dio emission generated by terrestrial planets inside the habitable zone of M, K, G and F stars
 could be lower than expected.

The less restrictive conditions to the exoplanet habitability are linked to a radio emis-
 sion signal with rather low variability. This is the case for simulations with low SW dynamic
 pressure and IMF intensity, that is to say, space weather conditions leading to magnetopause
 standoff distances further away from the exoplanet surface.

The inference of the the magnetic field intensity and topology of exoplanets may need
 long periods of observational data if one wishes to isolate the effect of the space weather con-
 ditions on the radio emission signal. The data filtering could be particularly challenging for
 the case of exoplanets exposed to recurrent extreme space weather conditions or a dominant
 IMF pressure, leading to a large radio emission variability. On the other hand, the identifica-

tion of the magnetic field characteristics for exoplanets facing more benign space weather conditions could be less complex, because the variability of the radio emission data should be smaller.

Once the properties of the exoplanet magnetic field are identified, the analysis of the radio emission time series opens the possibility of tracking the space weather conditions on the exoplanet orbit, providing important information about the host star as the magnetic field or SW dynamic pressure.

5 Conclusions and discussion

Present study is dedicated to analyze the interaction between the stellar wind and exoplanets with an Earth-like magnetosphere hosted by M stars and F star type τ Boo, in particular the habitability restrictions induced by the sterilizing effect of the stellar wind on the exoplanet surface if the magnetosphere shielding is inefficient. The radio emission generated by exoplanets with an Earth-like magnetosphere is also calculated for different space weather conditions. With that aim, a set of MHD simulations were performed reproducing the interaction of the stellar wind with the exoplanet magnetosphere during regular and extreme space weather conditions.

The simulations results indicate that exoplanets with an Earth-like magnetosphere hosted by a M star at 0.2 au are protected from the stellar wind during regular and CME-like space weather conditions. This protection holds if the rotation period of the star is 3 days or larger, although fast rotators can constrain the exoplanet habitability due to the generation of intense and recurrent CME-like events (?). Likewise, if the exoplanet orbit is at 0.1 au, the magnetosphere protection only holds for M stars with a rotation period of 12 days or larger. On the other hand, if the exoplanet orbit is below 0.1 au, the magnetic field must be stronger regarding the Earth to avoid the direct impact of the stellar wind at low latitudes, particular during CME-like space weather conditions. It should be noted that the discussion about the properties of the terrestrial exoplanet magnetic fields, for example the type of internal magnetic dynamo at different orbits, the spinning rotation speed or the synchronicity with the host star are not explored in this study, although these effects must be consider to improve the accuracy of the predictions (?).

If the exoplanet is hosted by a F stars like τ Boo inside the habitable zone, regular space weather conditions do not impose strong constraint on the habitability. On the other hand, if the exoplanet orbit is close to the inner boundary of the habitable zone (2.5 au), an efficient shielding during CME-like space weather conditions requires a stronger magnetic field compared to the Earth. The introduction of the effect of the star rotation in the analysis indicates that the direct precipitation of the SW can occur if the star rotation period is below 10 days for exoplanets at 2.5 au during extreme space weather conditions, although for exoplanets at 5 au the star rotation period must be 2 days or lower.

The radio emission calculated in simulations with a dynamic pressure between $P_d = 2.5\text{--}14$ nPa shows the same order of magnitude regarding the scaling proposed by ? (?), predicting $7.5 \cdot 10^7$ W. That is to say, the radio emission obtained in the simulations is consistent with the scaling during regular and weak CME-like space weather conditions. Likewise, simulations with fixed dynamic pressure ($P_d = 1.2$ nPa) also show radio emission values comparable with ? (?) scaling if the IMF intensity is in the range of values observed during regular to strong CME-like space weather conditions. In addition, the southward IMF orientation leads to the strongest radio emission and the northward IMF to the lowest. The simulations indicate an enhancement of the radio emission as the stellar wind dynamic pressure and IMF intensity increase. Consequently, radio telescopes may receive a stronger signal from exoplanets hosted by stars with large magnetic activity and intense stellar wind (high SW density and velocity), particularly if the exoplanet orbit is close to the star. Nevertheless, such adverse space weather conditions requires an exoplanet with a intense magnetic field that avoids the collapse of the magnetopause on the exoplanet surface. Such ensemble of space weather and exoplanet

628 magnetic field characteristics are found in Hot Jupiters, reason why the first potential detec-
 629 tion of radio emission from an exoplanet involved the Hot Jupiter τ Boo b (? , ?). Unfortunately,
 630 the radio emission detection from exoplanets hosted by stars with more favorable habitabil-
 631 ity conditions regarding the space weather inside habitable zone, will require a new genera-
 632 tion of radio telescopes with improved resolution and sensibility because the radio emission
 633 signal should be several orders of magnitude smaller compared to Hot Jupiters.

634 The simulations indicate a larger variability of the exoplanet radio emission induced by
 635 the IMF orientation if the bow shock does not exist, that is to say, the stellar wind dynamic
 636 pressure is low enough and the IMF intensity high enough to be in the parametric range of
 637 $M_A < 1$. On the other hand, the radio emission variability caused by the IMF orientation is
 638 smaller if the bow shock exist ($M_A > 1$). That happens because, if the bow shock exist, there
 639 is a component of the radio emission linked to the compression and bending of the IMF lines
 640 in the nose of the bow shock, mainly dependent on the dynamic pressure of the stellar wind.
 641 Thus, the radio emission sources are the bow shock compression and the reconnection site be-
 642 tween IMF and exoplanet magnetic field. Consequently, the role of the IMF orientation is smaller
 643 with respect to the configurations without bow shock. The implication of this result is that ex-
 644 oplanet magnetospheres routinely perturbed by intense IMF avoiding the formation of the bow
 645 shock ($M_A < 1$) may show a larger radio emission variability with respect to exoplanet mag-
 646 netospheres with a bow shock. That is to say, if the exoplanet is hosted by a star with strong
 647 magnetic activity although relative low stellar wind dynamic pressure, the radio telescopes may
 648 measure a large time variability induced by changes in the IMF orientation, particularly if the
 649 magnetosphere erosion leads to a magnetopause located close to the exoplanet surface. Hence,
 650 if radio telescopes routinely measure relatively strong and very variable signal, the exoplanet
 651 habitability conditions may not be optimal from the point of view of the space weather and
 652 the exoplanet magnetic field intensity. The same way, if the host star has a relative weak mag-
 653 netic activity although generates intense stellar winds (large dynamic pressure), the radio emis-
 654 sion detected must be relatively large and show a small variability, pointing out a large com-
 655 pression of the exoplanet magnetosphere and low magnetopause standoff distances, thus the
 656 exoplanet habitability state regarding the space weather conditions and the intrinsic magnetic
 657 field is less favorable. Therefore, the combination of low radio emission and small variabil-
 658 ity may indicate the space weather conditions and the intrinsic magnetic field of the exoplanet
 659 support lower limitations for the exoplanet habitability, efficiently shield by the magnetosphere
 660 from the sterilizing effect of the stellar wind.

661 The analysis of the simulations combining the effect of the SW dynamic pressure with
 662 the IMF orientation and intensity shows radio emission values between $3 \cdot 10^7$ W for com-
 663 mon CME up to $2 \cdot 10^{10}$ W for super CME. The simulations with large SW dynamic pres-
 664 sure and IMF intensity leads to an enhancement of the radio emission because the bow shock
 665 is strongly compressed, the reconnection between the IMF and the exoplanet magnetic field
 666 is strong and the magnetopause is located close to the exoplanet surface. The statistical anal-
 667 ysis shows similar radio emission trends with respect to the SW dynamic pressure and IMF
 668 intensity, although the scaling is slightly affected by the IMF orientation. In particular, the south-
 669 ward IMF leads to the largest IMF intensity dependency, 20% larger with respect to the SW
 670 dynamic pressure trend.

Statistical analysis of the radio emission calculated in the simulations leads to data re-
 gression exponents that deviate with respect to the radio-magnetic scaling laws (? , ? , ?). Nev-
 ertheless, the agreement improves comparing the radio-magnetic scaling law of a configura-
 tion with dominant IMF pressure and the data regression for a Southward IMF orientation. Con-
 sequently, the trends of radio-magnetic scaling law and simulations are similar if the bow shock
 does not exist and the IMF is perpendicular to the SW velocity. That means the radio-magnetic
 scaling laws does not fully capture the effect of the bow shock compression and magnetosphere
 distortion on the radio emission generation due to the combined effect of the SW and IMF.
 The scaling law obtained from the simulation is, including the range of exponent values cal-

culated for different IMF orientations:

$$P_w \propto |B|_{IMF}^{(0.9-1.22)} P_d^{(0.95-1.15)}$$

671 that is to say, the radio-magnetic scaling law for space weather conditions with a dominant
 672 SW pressure could overestimate the trend of the IMF intensity ($P_w \propto |B_{IMF,\perp}|^2$) and under-
 673 estimate the trend of the SW dynamic pressure ($P_w \propto P_d^{0.17}$). On the other hand, the predic-
 674 tion of the radio-magnetic scaling law for space weather conditions with a dominant IMF pres-
 675 sure is closer to the simulations scaling regarding the IMF intensity ($P_w \propto |B_{IMF,\perp}|^{1.3}$) and
 676 the SW dynamic pressure $P_w \propto P_d^{0.5}$). In summary, the theoretical scaling may underestimate
 677 the radio emission generation, particularly with respect to the SW dynamic pressure trend.

678 A further refinement of the simulations scaling requires an improved description of the
 679 model's physics, for example introducing the exoplanet rotation and kinetic effects. Neverthe-
 680 less, the present study provides a first order approximation of the exoplanet standoff distance
 681 and magnetospheric radio emission with respect to the space weather conditions generated by
 682 host star.

683 Appendix A Numerical model validation

684 The numerical model used in this study was also applied in the analysis of the interac-
 685 tion between the solar wind and the Earth magnetosphere (Liu et al., 2020). Part of Liu et al. (2020) study was ded-
 686 icated to analyze the perturbation induced in the magnetosphere by several CMEs that impacted
 687 the Earth from 1997 to 2020. The simulations results were compared with observational data
 688 to validate the numerical model, in particular the K_p index. The K_p index provides the global
 689 geomagnetic activity taking values from 0 if the geomagnetic activity is weak to 9 if the geo-
 690 magnetic activity is extreme (Liu et al., 2020). The K_p index was calculated in the simulations as the
 691 lowest latitude with open magnetic field lines in the Earth surface at the North Hemisphere.
 692 Figure A1 shows the correlation between the K_p index obtained in the simulations with re-
 693 spect to the measured values. The statistical analysis finds a correlation coefficient of 0.83, that
 694 is to say, a reasonable agreement between simulations and observational data. Consequently,
 695 the numerical model is valid to reproduce the global structures of the Earth magnetosphere
 696 during extreme space weather conditions, also suitable to analyze the interaction of the stel-
 697 lar wind with exoplanet magnetospheres if the intrinsic magnetic field is similar to the Earth.

698 Appendix B Calculation of the magnetopause standoff distance

The theoretical approximation of the magnetopause standoff distance is calculated as the
 balance between the dynamic pressure of the SW ($P_d = m_p n_{sw} v_{sw}^2 / 2$), the thermal pressure
 of the SW ($P_{th,sw} = m_p n_{sw} v_{th,sw}^2 / 2 = m_p n_{sw} c_{sw}^2 / \gamma$), and the magnetic pressure of the IMF
 ($P_{mag,sw} = B_{sw}^2 / (2\mu_0)$) with respect to the magnetic pressure of a dipolar magnetic field ($P_{mag,ex} =$
 $\alpha \mu_0 M_{ex}^2 / 8\pi^2 r^6$) and the thermal pressure of the magnetosphere ($P_{th,MSP} = m_p n_{MSP} v_{th,MSP}^2 / 2$).
 This results in the expression:

$$P_d + P_{mag,sw} + P_{th,sw} = P_{mag,ex} + P_{th,MSP} \quad (B1)$$

$$\frac{R_{mp}}{R_{ex}} = \left[\frac{\alpha \mu_0 M_{ex}^2}{4\pi^2 \left(m_p n_{sw} v_{sw}^2 + \frac{B_{sw}^2}{\mu_0} + \frac{2m_p n_{sw} c_{sw}^2}{\gamma} - m_p n_{MSP} v_{th,MSP}^2 \right)} \right]^{(1/6)} \quad (B2)$$

699 with M_{ex} the exoplanet dipole magnetic field moment, $r = R_{mp}/R_{ex}$, and α the dipole com-
 700 pression coefficient ($\alpha \approx 2$ (Liu et al., 2020)). This approximation does not include the effect of the re-
 701 connections between the IMF with the exoplanet magnetic fields, thus the expression assumes
 702 a compressed dipolar magnetic field, ignoring the orientation of the IMF. Here, the approx-
 703 imation is only valid if the IMF intensity is rather low and the magnetopause standoff distance
 704 should be calculated using simulations for extreme space weather conditions.

The magnetopause standoff distance is defined in the simulations analysis as the last close magnetic field line on the exoplanet dayside at 0° longitude in the ecliptic plane.

Acknowledgments

This work was supported by the project 2019-T1/AMB-13648 founded by the Comunidad de Madrid. The research leading to these results has received funding from the grants ERC Whole-Sun 810218, Exoplanets A and INSU/PNP. We extend our thanks to CNES for Solar Orbiter, PLATO and Space weather science support and to INSU/PNST for their financial support. This work has been supported by Comunidad de Madrid (Spain) - multiannual agreement with UC3M (“Excelencia para el Profesorado Universitario” - EPUC3M14) - Fifth regional research plan 2016-2020. P. Zarka acknowledges funding from the ERC No 101020459 - Exoradio). Data available on request from the authors.

References

- Aarnio, A. N., Matt, S. P., & Stassun, K. G. (2012). Mass loss in pre-main sequence stars via coronal mass ejections and implications for angular momentum loss. *The Astrophysical Journal*, 760(1), 9.
- Airapetian, V. S., Barnes, R., Cohen, O., Collinson, G. A., Danchi, W. C., Dong, C. F., ... et al. (2020). Impact of space weather on climate and habitability of terrestrial-type exoplanets. *International Journal of Astrobiology*, 19(2), 136–194.
- Bailey, J. D. (2014). Measuring the surface magnetic fields of magnetic stars with unresolved zeeman splitting. *A&A*, 568, A38.
- Barnes, R. (2017). Tidal locking of habitable exoplanets. *Celestial Mechanics and Dynamical Astronomy*, 129(4), 509-536.
- Benjamin J. S., Pope, B. J. S., Bedell, M., Callingham, J. R., Vedantham, H. K., Snellen, T., ... Shimwell, T. W. (2020). No massive companion to the coherent radio-emitting m dwarf GJ 1151. *The Astrophysical Journal*, 890(2), L19.
- Brun, A. S., Strugarek, A., Noraz, Q., Perri, B., Varela, J., Augustson, K., ... Toomre, J. (2022). Powering stellar magnetism: Energy transfers in cyclic dynamos of sun-like stars. *The Astrophysical Journal*, 926(1), 21.
- Cane, H. V., & Richardson, I. G. (2003). Interplanetary coronal mass ejections in the near-earth solar wind during 1996–2002. *Journal of Geophysical Research: Space Physics*, 108(A4), 1-13.
- Carilli, C. L., & Rawlings, S. (2004). Science with the square kilometer array: Motivation, key science projects, standards and assumptions. *New Astronomy Reviews*, 48, 979-984.
- Cuntz, M., & Guinan, E. F. (2016). About exobiology: The case for dwarf k stars. *The Astrophysical Journal*, 827(1), 79.
- Facsó, G., Honkonen, I., Živković, T., Palin, L., Kallio, E., Ågren, K., ... Milan, S. (2016). One year in the earth’s magnetosphere: A global mhd simulation and spacecraft measurements. *Space Weather*, 14(5), 351-367.
- Fares, R., Donati, J.-F., Moutou, C., Bohlender, D., Catala, C., Deleuil, M., ... Walker, G. A. H. (2009). Magnetic cycles of the planet-hosting star bootis – ii. a second magnetic polarity reversal. *Monthly Notices of the Royal Astronomical Society*, 398(3), 1383-1391.
- Fares, R., Moutou, C., Donati, J., Catala, C., Shkolnik, E. L., Jardine, M. M., ... Deleuil, M. (2013). A small survey of the magnetic fields of planet-host stars. *Monthly Notices of the Royal Astronomical Society*, 435(2), 1451-1462.
- Gallet, F., Charbonnel, C., Amard, L., Brun, S., Palacios, A., & Mathis, S. (2017). Impacts of stellar evolution and dynamics on the habitable zone: The role of rotation and magnetic activity. *A&A*, 597, A14.
- Garraffo, C., Drake, J. J., & Cohen, O. (2016). The space weather of proxima centauri b. *The Astrophysical Journal*, 833(1), L4.

- 756 Garraffo, C., Drake, J. J., Cohen, O., Alvarado-Gómez, J. D., & Moschou, S. P. (2017). The
757 threatening magnetic and plasma environment of the TRAPPIST-1 planets. *The Astro-*
758 *physical Journal*, 843(2), L33.
- 759 Gombosi, T. I. (1994). *Gaskinetic theory*. Cambridge University Press.
- 760 González Hernández, I., Komm, R., Pevtsov, A., & Leibacher, J. (2014). *Solar origins of*
761 *space weather and space climate*. Springer-Verlag New York.
- 762 Griebmeier, J.-M., Stadelmann, A., Motschmann, U., Belisheva, N.K., Lammer, H., & Bier-
763 nat, H.K. (2005). Cosmic ray impact on extrasolar earth-like planets in close-in
764 habitable zones. *Astrobiology*, 5(5), 587-603.
- 765 Griebmeier, J.-M., Stadelmann, A., Penz, T., Lammer, H., Selsis, F., Ribas, I., ... Weiss,
766 W. W. (2004). The effect of tidal locking on the magnetospheric and atmospheric
767 evolution of "hot jupiters". *A&A*, 425(2), 753-762.
- 768 Hapgood, M. (2019). The great storm of may 1921: An exemplar of a dangerous space
769 weather event. *Space Weather*, 17(7), 950-975.
- 770 Hess, S. L. G., & Zarka, P. (2011). Modeling the radio signature of the orbital parameters,
771 rotation, and magnetic field of exoplanets. *Astron. Astrophys.*, 531(4), A29.
- 772 Howard, R.A. (2006). A historical perspective on coronal mass ejections. In *Solar eruptions*
773 *and energetic particles* (p. 7-13). American Geophysical Union (AGU). doi: <https://doi.org/10.1029/165GM03>
774
- 775 Hu, Y., & Yang, J. (2014). Role of ocean heat transport in climates of tidally locked exoplanets
776 around m dwarf stars. *Proceedings of the National Academy of Sciences*, 111(2),
777 629-634.
- 778 Jakosky, B. M., Grebowsky, J. M., Luhmann, J. G., & Brain, D. A. (2015). Initial results
779 from the maven mission to mars. *Geophysical Research Letters*, 42(21), 8791-8802.
- 780 Jia, X., Slavin, J. A., Gombosi, T. I., Daldorff, L. K. S., Toth, G., & Holst, B. (2015). Global
781 MHD simulations of Mercury's magnetosphere with coupled planetary interior: In-
782 duction effect of the planetary conducting core on the global interaction. *Journal of*
783 *Geophysical Research (Space Physics)*, 120(6), 4763-4775.
- 784 Johnstone, C. P., Güdel, M., Brott, I., & Lüftinger, T. (2015). Stellar winds on the main-
785 sequence - ii. the evolution of rotation and winds. *A&A*, 577, A28.
- 786 Johnstone, C. P., Güdel, M., Lüftinger, T., Toth, G., & Brott, I. (2015). Stellar winds on the
787 main-sequence - i. wind model. *A&A*, 577, A27.
- 788 Kabin, K., Heimpel, M. H., Rankin, R., Aurnou, J. M., Gómez-Pérez, N., Paral, J., ...
789 DeZeeuw, D. L. (2008). Global MHD modeling of Mercury's magnetosphere with
790 applications to the MESSENGER mission and dynamo theory. *Icarus*, 195(1), 1-15.
- 791 Kaiser, M. L., & Desch, M. D. (1984). Radio emissions from the planets earth, jupiter, and
792 saturn. *Reviews of Geophysics*, 22, 373.
- 793 Kasting, J. F., Whitmire, D. P., & Reynolds, R. T. (1993). Habitable zones around main se-
794 quence stars. *Icarus*, 101(1), 108-128.
- 795 Khodachenko, M. L., Ribas, I., Lammer, H., Griebmeier, J. M., Leitner, M., Selsis, F., ...
796 Rucker, H. O. (2007). Coronal mass ejection (cme) activity of low mass m stars as an
797 important factor for the habitability of terrestrial exoplanets. i. cme impact on expected
798 magnetospheres of earth-like exoplanets in close-in habitable zones. *Astrobiology*,
799 7(1), 167-184.
- 800 Kilpua, E.K.J., Lugaz, N., Mays, M. L., & Temmer, M. (2019). Forecasting the structure and
801 orientation of earthbound coronal mass ejections. *Space Weather*, 17(4), 498-526.
- 802 Kopparapu, R. K., Ramirez, R., Kasting, J. F., Eymet, V., Robinson, T. D., Mahadevan, S., ...
803 Deshpande, R. (2013). Habitable zones around main-sequence stars: New estimates.
804 *The Astrophysical Journal*, 765(2), 131.
- 805 Kopparapu, R. K., Ramirez, R. M., SchottelKotte, J., Kasting, J. F., Domagal-Goldman, S.,
806 & Eymet, V. (2014). Habitable zones around main-sequence stars: Dependence on
807 planetary mass. *The Astrophysical Journal*, 787(2), L29.
- 808 Lammer, H., Lichtenegger, I. M., Kulikov, Y. N., Griebmeier, J. M., Terada, N., Erkaev,
809 N. V., ... Selsis, F. (2007). Coronal mass ejection (cme) activity of low mass m stars
810 as an important factor for the habitability of terrestrial exoplanets. ii. cme-induced

- 811 ion pick up of earth-like exoplanets in close-in habitable zones. *Astrobiology*, 7(1),
812 85-207.
- 813 Lamy, L., Zarka, P., Cecconi, B., Klein, L., Masson, S., Denis, L., ... Viou, C. (2017). 1977-
814 2017 : 40 years of decametric observations of jupiter and the sun with the nançay
815 decameter array. , 455-466.
- 816 Leconte, J., Wu, H., Menou, K., & Murray, N. (2015). Asynchronous rotation of earth-mass
817 planets in the habitable zone of lower-mass stars. *Science*, 347(6222), 632-635.
- 818 Leitzinger, M., Odert, P., Greimel, R., Vida, K., Kriskovics, L., Guenther, E. W., ... Lam-
819 mer, H. (2020). A census of coronal mass ejections on solar-like stars. *Monthly*
820 *Notices of the Royal Astronomical Society*, 493(3), 4570-4589.
- 821 Linsky, J. (2019). Space weather: The effects of host star flares on exoplanets. In *Host*
822 *stars and their effects on exoplanet atmospheres : An introductory overview* (Vol. 955,
823 p. 229-242). Springer International Publishing.
- 824 Low, B. C. (2001). Coronal mass ejections, magnetic flux ropes, and solar magnetism. *Jour-*
825 *nal of Geophysical Research: Space Physics*, 106(A11), 25141-25163.
- 826 Lugaz, N., Farrugia, C. J., Huang, C.-L., & Spence, H. E. (2015). Extreme geomagnetic
827 disturbances due to shocks within cmes. *Geophysical Research Letters*, 42(12), 4694-
828 4701.
- 829 Lundin, R., Lammer, H., & Ribas, I. (2007). Planetary magnetic fields and solar forcing: Im-
830 plications for atmospheric evolution. *Space Science Reviews*, 129(1), 245-278.
- 831 Marsden, S. C., Petit, P., Jeffers, S. V., Morin, J., Fares, R., Reiners, A., ... the BCool Col-
832 laboration (2014). A bcool magnetic snapshot survey of solar-type stars. *Monthly*
833 *Notices of the Royal Astronomical Society*, 444, 3517-3536.
- 834 Mathur, S., García, R. A., Ballot, J., Ceillier, T., Salabert, D., Metcalfe, T. S., ... Bloemen,
835 S. (2014). Magnetic activity of f stars observed by kepler. *A&A*, 562, A124.
- 836 Matt, S. P., Brun, A. S., Baraffe, I., Bouvier, T., & Chabrier, G. (2015). THE MASS-
837 DEPENDENCE OF ANGULAR MOMENTUM EVOLUTION IN SUN-LIKE
838 STARS. *The Astrophysical Journal*, 799(2), L23.
- 839 Menvielle, M., & Berthelier, A. (1991). The k-derived planetary indices: Description and
840 availability. *Reviews of Geophysics*, 29(3), 415-432.
- 841 Mignone, A., Bodo, G., Massaglia, S., Matsakos, T., Tesileanu, O., Zanni, C., & Ferrari, A.
842 (2007). Pluto: A numerical code for computational astrophysics. *ApJS*, 170, 228-242.
- 843 Moore, T. E., & Khazanov, G. V. (2010). Mechanisms of ionospheric mass escape. *Journal*
844 *of Geophysical Research: Space Physics*, 115(A12), A00J13.
- 845 Nan, R., Li, D., Jin, C., Wang, Q., Zhu, L., Zhu, W., ... Qian, L. (2011). The five hundred
846 meter aperture spherical radio telescope (fast) project. *International Journal of Mod-*
847 *ern Physics D*, 20, 989-1024.
- 848 Neugebauer, M., & Goldstein, R. (1997). Particle and field signatures of coronal mass
849 ejections in the solar wind. *Washington DC American Geophysical Union Geophysical*
850 *Monograph Series*, 99, 245-251.
- 851 Newton, E. R., Mondrik, N., Irwin, J., Winters, J. G., & Charbonneau, D. (2018). New
852 rotation period measurements for m dwarfs in the southern hemisphere: An abundance
853 of slowly rotating, fully convective stars. *The Astronomical Journal*, 156(5), 217.
- 854 Nielsen, M. B., Gizon, L., Schunker, H., & Karoff, C. (2013). Rotation periods of 12 main-
855 sequence kepler stars: Dependence on stellar spectral type and comparison with $v \sin i$
856 observations. *A&A*, 55, L10.
- 857 Odstrcil, D., & Pizzo, V. J. (1999). Three-dimensional propagation of coronal mass ejections
858 (cmes) in a structured solar wind flow: 1. cme launched within the streamer belt. *Jour-*
859 *nal of Geophysical Research: Space Physics*, 104(A1), 483-492.
- 860 Odstrcil, D., Riley, P., & Zhao, X. P. (2004). Numerical simulation of the 12 may 1997 inter-
861 planetary cme event. *Journal of Geophysical Research: Space Physics*, 109(A2).
- 862 Pérez-Torres, M., Gómez, J. F., Ortiz, J. L., Leto, P., Anglada, G., Gómez, J. L., ...
863 Chibueze, J. (2021). Monitoring the radio emission of proxima centauri. *A&A*,
864 645, A77.
- 865 Perger, M., Ribas, I., Anglada-Escudé, G., Morales, J. C., Amado, P. J., Caballero, J. A., ...

- 866 Zechmeister, M. (2021). The carmenes search for exoplanets around m dwarfs - no
867 evidence for a super-earth in a 2-day orbit around gj 1151. *A&A*, 649, L12.
- 868 Popinchalk, M., Faherty, J. K., Kiman, R., Gagne, J., Curtis, J. L., Angus, R., . . . Rice, E. L.
869 (2021). Evaluating rotation periods of m dwarfs across the ages. *The Astrophysical*
870 *Journal*, 916(2), 77.
- 871 Poppe, B.B., & Jorden, K.P. (2006). *Sentinels of the sun: Forecasting space weather*. John-
872 son Books.
- 873 Raeder, J., McPherron, R. L., Frank, L. A., Kokubun, S., Lu, G., Mukai, T., . . . Slavin, J. A.
874 (2001). Global simulation of the geospace environment modeling substorm challenge
875 event. *Journal of Geophysical Research: Space Physics*, 106(A1), 381-395.
- 876 Regnault, F., Janvier, M., Demoulin, P., Auchere, F., Strugarek, A., Dasso, S., & Nous, C.
877 (2020). 20 years of ace data: How superposed epoch analyses reveal generic features
878 in interplanetary cme profiles. *Journal of Geophysical Research: Space Physics*,
879 125(11), e2020JA028150.
- 880 Ricci, L., Liu, S.-F., Isella, A., & Li, H. (2018). Investigating the early evolution of planetary
881 systems with alma and the next generation very large array. *Astrophys. J.*, 853, 110.
- 882 Saffe, C., Gómez, M., & Chavero, C. (2005). On the ages of exoplanet host stars. *A&A*,
883 443(2), 609-626.
- 884 Salman, T. M., Lugaz, N., Farrugia, C. J., Winslow, R. M., Galvin, A. B., & Schwadron,
885 N. A. (2018). Forecasting periods of strong southward magnetic field following
886 interplanetary shocks. *Space Weather*, 16(12), 2004-2021.
- 887 Sato, S., Cuntz, M., Guerra Olvera, C. M., Jack, D., & Schroder, K.-P. (2014). Habitability
888 around f-type stars. *International Journal of Astrobiology*, 13(3), 244-258.
- 889 Scalo, J., Kaltenecker, L., Segura, A., Fridlund, M., Ribas, I., Kulikov, Y. N., . . . Lammer, H.
890 (2007). M stars as targets for terrestrial exoplanet searches and biosignature detection.
891 *Astrobiology*, 7(1), 85-166.
- 892 Seach, J. M., Marsden, S. C., Carter, D. B., Neiner, C., Folsom, C. P., Mengel, M. W., . . .
893 Buyschaert, B. (2020). A magnetic snapshot survey of f-type stars. *Monthly Notices*
894 *of the Royal Astronomical Society*, 494, 5682-5703.
- 895 See, V., Matt, S. P., Folsom, C. P., Saikia, S. B., Donati, J.-F., Fares, R., . . . Waite, I. A.
896 (2019). Estimating magnetic filling factors from zeeman-doppler magnetograms. *The*
897 *Astrophysical Journal*, 876(2), 118.
- 898 Shields, Aomawa L., Ballard, S., & Johnson, J. A. (2016). The habitability of planets orbit-
899 ing m-dwarf stars. *Physics Reports*, 663, 1-38.
- 900 Shoda, M., Suzuki, T. K., Matt, S. P., Cranmer, S. R., Vidotto, A. A., Strugarek, A., . . . Brun,
901 A. S. (2020). Alfvén-wave-driven magnetic rotator winds from low-mass stars. i. rota-
902 tion dependences of magnetic braking and mass-loss rate. *The Astrophysical Journal*,
903 896(2), 123.
- 904 Shulyak, D., Reiners, A., Engeln, A., Malo, L., Yadav, R., Morin, J., & Kochukhov, O.
905 (2017). Strong dipole magnetic fields in fast rotating fully convective stars. *Nature*
906 *Astronomy*, 1(8), 0184.
- 907 Shulyak, D., Reiners, A., Nagel, E., Tal-Or, L., Caballero, J. A., Zechmeister, M., . . . Pedraz,
908 S. (2019). Magnetic fields in m dwarfs from the carmenes survey. *A&A*, 626, A86.
- 909 Stevenson, D. J. (2003). Planetary magnetic fields. *Earth and Planetary Science Letters*,
910 208(1), 1-11.
- 911 Strugarek, A., Brun, A. S., Matt, S. P., & Réville, V. (2014). On the diversity of magnetic in-
912 teractions in close-in star-planet systems. *apj*, 795(1), 86.
- 913 Strugarek, A., Brun, A. S., Matt, S. P., & Réville, V. (2015). Magnetic Games between a
914 Planet and Its Host Star: The Key Role of Topology. *apj*, 815(2), 111.
- 915 Suzuki, T.K. (2013). Evolution of solar-type stellar winds. *Astronomische Nachrichten*,
916 334(1-2), 81-84.
- 917 Tarter, J. C., Backus, P. R., Mancinelli, R. L., Aurnou, J. M., Backman, D. E., Basri, G. S.,
918 . . . Young, R. E. (2007). A reappraisal of the habitability of planets around m dwarf
919 stars. *Astrobiology*, 7(1), 30-65.

- 920 Thomsen, M. F. (2004). Why k_p is such a good measure of magnetospheric convection.
921 *Space Weather*, 2(11), S11004.
- 922 Turner, J. D., Zarka, P., Griessmeier, J. M., Lazio, J., Cecconi, B., Emilio Enriquez, J., ...
923 de Pater, I. (2021). The search for radio emission from the exoplanetary systems 55
924 cancri, ν andromedae, and τ bootis using lofar beam-formed observations. *A&A*, 645,
925 A59.
- 926 van Haarlem, M. P., Wise, M. W., Gunst, A. W., Heald, G., McKean, J. P., Hessels, J. W. T.,
927 ... van Zwieten, J. (2013). Lofar: The low-frequency array. *A&A*, 556, A2.
- 928 Varela, J., Pantellini, F., & Moncuquet, M. (2015). The effect of interplanetary magnetic field
929 orientation on the solar wind flux impacting mercurys surface. *Planet. Space Sci.*, 119,
930 264-269.
- 931 Varela, J., Pantellini, F., & Moncuquet, M. (2016a). Effect of the interplanetary magnetic
932 field orientation and intensity in the mass and energy deposition on the Hermean
933 surface. *Planet. Space Sci.*, 129, 74-87.
- 934 Varela, J., Pantellini, F., & Moncuquet, M. (2016b). Parametric study of the solar wind
935 interaction with the hermean magnetosphere for a weak interplanetary magnetic field.
936 *Planet. Space Sci.*, 120, 78-86.
- 937 Varela, J., Pantellini, F., & Moncuquet, M. (2016c). Plasma streams in the Hermean dayside
938 magnetosphere: Solar wind injection through the reconnection region. *Planet. Space
939 Sci.*, 122, 46-52.
- 940 Varela, J., Reville, V., Brun., A. S., Pantellini, F., & Zarka, P. (2016). Radio emission in mer-
941 cury magnetosphere. *A&A*, 595, A69.
- 942 Varela, J., Reville, V., Brun, A. S., Zarka, P., & Pantellini, F. (2018). Effect of the exoplanet
943 magnetic field topology on its magnetospheric radio emission. *A&A*, 616, A182.
- 944 Varela, J., Reville, V., Brun, A. S., Zarka, P., & Pantellini, F. (2022). Mhd study of the
945 planetary magnetospheric response during extreme solar wind conditions: Earth and
946 exoplanet magnetospheres applications. *A&A*, 659, A10.
- 947 Vedantham, H. K., Callingham, J. R., Shimwell, T. W., Tasse, C., Pope, B. J. S., Bedell, M.,
948 ... White, G. J. (2020). Coherent radio emission from a quiescent red dwarf indicative
949 of star–planet interaction. *Nature Astronomy*, 4, 577.
- 950 Vidotto, A. A., Fares, R., Jardine, M., Donati, J.-F., Opher, M., Moutou, C., ... Gombosi,
951 T. I. (2012). The stellar wind cycles and planetary radio emission of the τ Boo system.
952 *MNRAS*, 423, 3285-3298.
- 953 Vidotto, A. A., Jardine, M., Morin, J., Donati, J. F., Opher, M., & Gombosi, T. I. (2013). M-
954 dwarf stellar winds: the effects of realistic magnetic geometry on rotational evolution
955 and planets. *Monthly Notices of the Royal Astronomical Society*, 438(2), 1162-1175.
- 956 Wang, Y. L., Raeder, J., Russell, C. T., Phan, T. D., & Manapat, M. (2003). Plasma deple-
957 tion layer: Event studies with a global model. *Journal of Geophysical Research: Space
958 Physics*, 108(A1), SMP 8-1-SMP 8-15.
- 959 Wang, Y. M., Ye, P. Z., Wang, S., & Xue, X. H. (2003). An interplanetary cause of large ge-
960 omagnetic storms: Fast forward shock overtaking preceding magnetic cloud. *Geophys-
961 ical Research Letters*, 30(13), 1-4.
- 962 Watanabe, K., & Sato, T. (1990). Global simulation of the solar wind-magnetosphere in-
963 teraction: The importance of its numerical validity. *Journal of Geophysical Research:
964 Space Physics*, 95(A1), 75-88.
- 965 Wu, C. S. (1979). A theory of the terrestrial kilometric radiation. , 230, 621.
- 966 Wu, C., & Lepping, R. P. (2015). Comparisons of characteristics of magnetic clouds and
967 cloud-like structures during 1995–2012. *Sol Phys*, 290(4), 1243-1269.
- 968 Yang, J., Cowan, N. B., & Abbot, D. S. (2013). Stabilizing cloud feedback dramatically ex-
969 pands the habitable zone of tidally locked planets. *The Astrophysical Journal*, 771(2),
970 L45.
- 971 Zarka, P. (1998). Auroral radio emissions at the outer planets : observations and theories. *J.
972 Geophys. Res.*, 103, 20159.
- 973 Zarka, P. (2007). Plasma interactions of exoplanets with their parent star and associated radio
974 emissions. *Planetary and Space Science*, 55(5), 598-617.

- 975 Zarka, P. (2018). Star-planet interactions in the radio domain: Prospect for their detection.
976 *Handbook of Exoplanets*, 1775-1790.
- 977 Zarka, P., Denis, L., Tagger, M., Girard, J., Coffre, A., Dumez-Viou, C.,
978 ... Corbel, S. (2020). The low-frequency radio telescope nenu-
979 far. *New Telescopes on the Frontier, Session J01, URSI GASS, Rome*,
980 <http://www.ursi.org/proceedings/procGA20/papers/URSIGASS2020SummaryPaperNenuFARnew.pdf>.
- 981
- 982 Zarka, P., Lazio, T. J. W., & Hallinan, G. (2015). Magnetospheric radio emissions from ex-
983 oplanets with the ska. *Proceedings of Advancing Astrophysics with the Square Kilome-*
984 *tre Array (AASKA14), Giardini Naxos, Italy*, <https://pos.sissa.it/215/120/pdf>, id.120.
- 985 Zarka, P., Treumann, R. A., Ryabov, B. P., & Ryabov, V. B. (2001). Magnetically-driven
986 planetary radio emissions and applications to extrasolar planets. *Astrophys. Space*
987 *Sci.*, 277, 293.

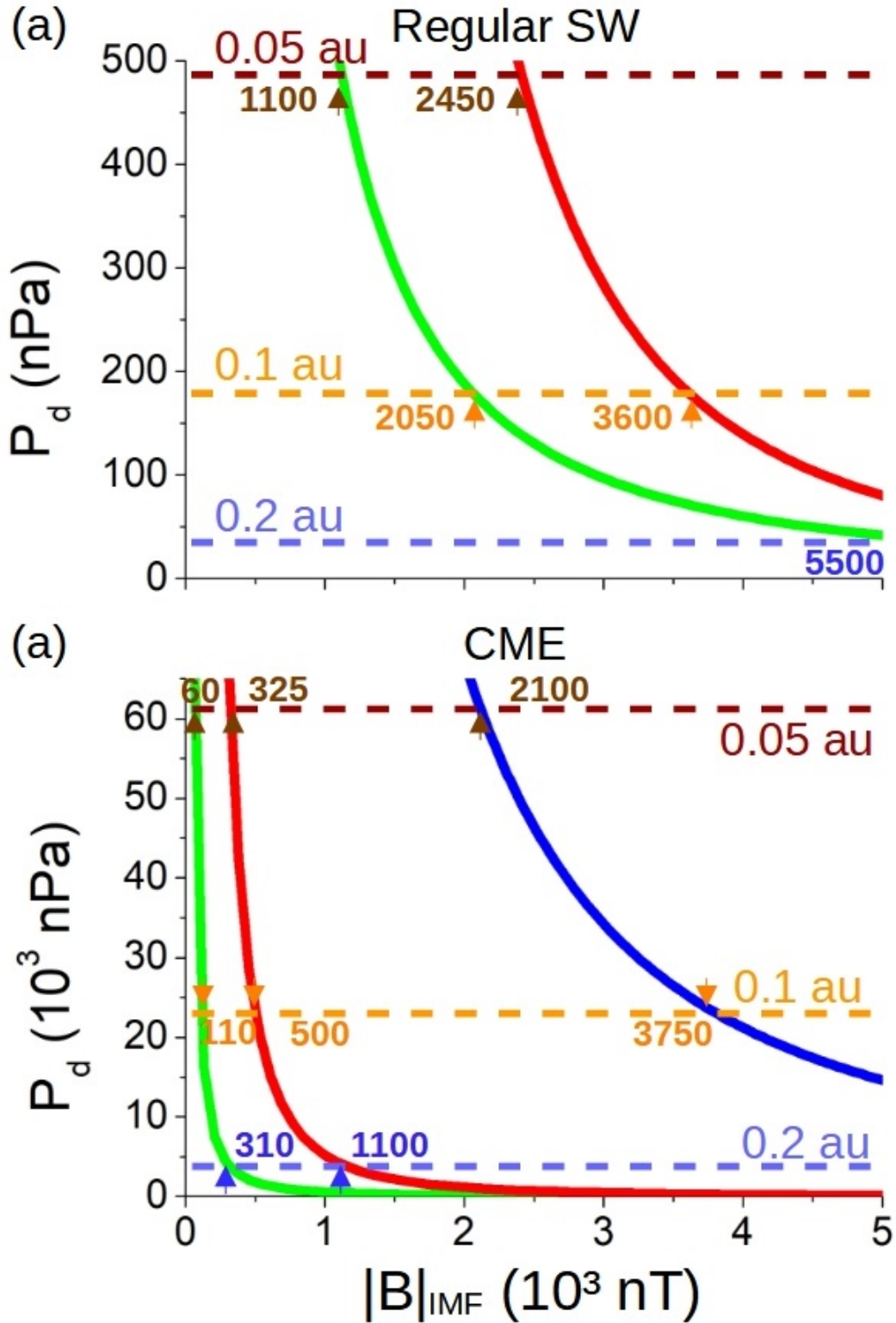
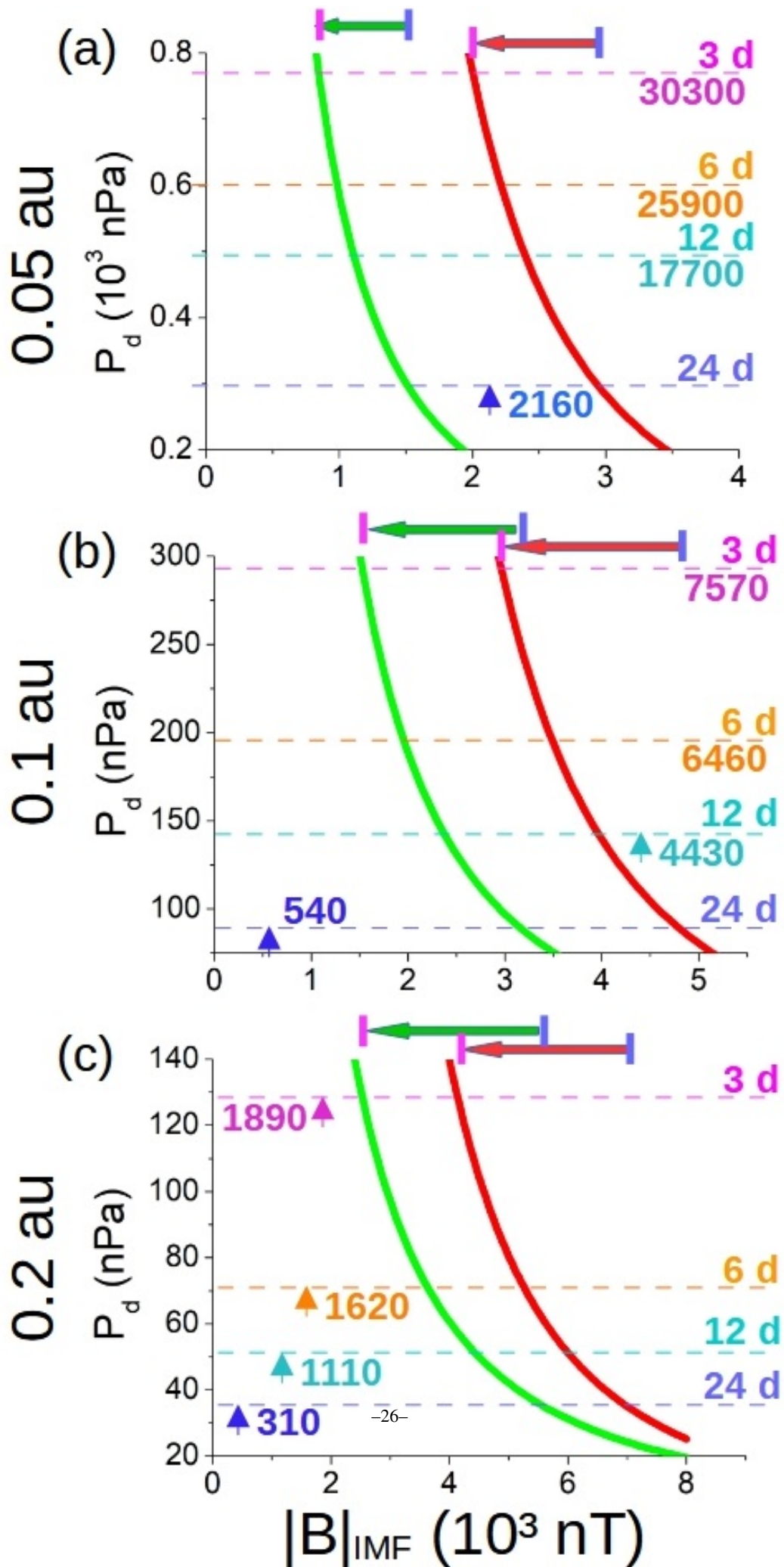


Figure 1. Critical IMF intensity and SW dynamic pressure required for the direct precipitation of the SW towards the exoplanet surface for (a) regular and (b) CME-like space weather conditions. IMF orientation: Exoplanet-star (red line), southward (green line) and northward (blue line). The horizontal dashed lines indicate the SW dynamic pressure at different exoplanet orbits: 0.05 au (red), 0.1 au (orange) and 0.2 au (blue). The critical IMF intensity is indicated for each IMF orientation.



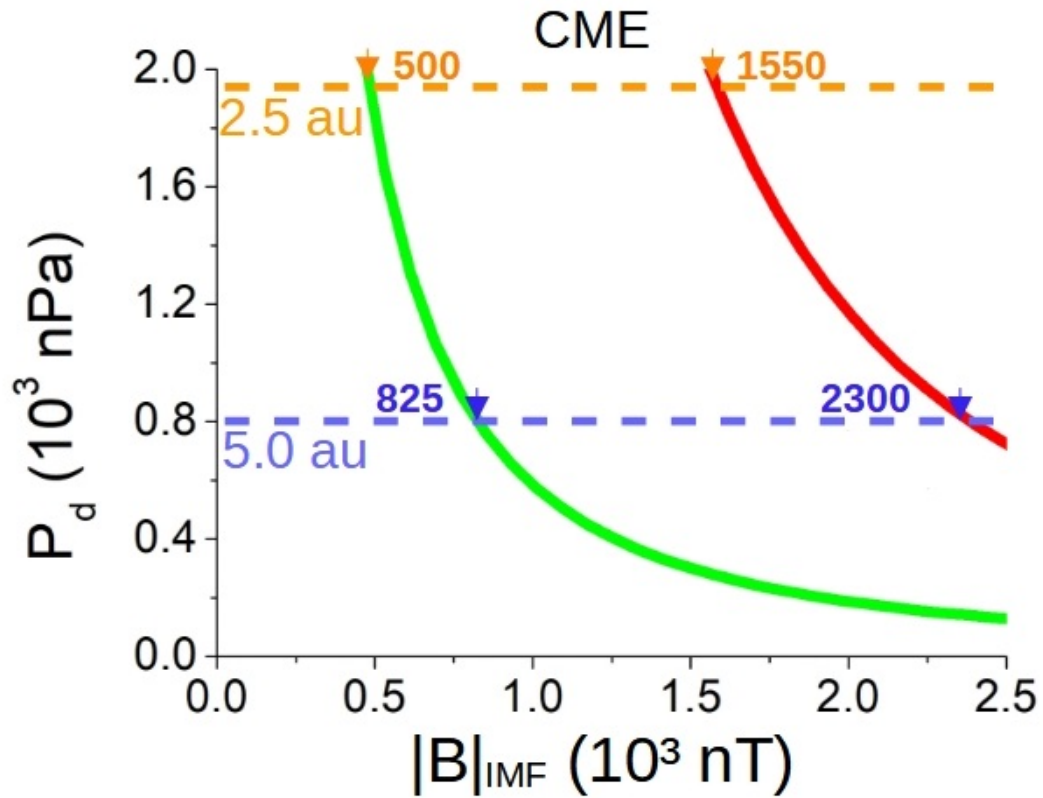


Figure 3. Critical IMF intensity and SW dynamic pressure required for the direct precipitation of the SW towards the exoplanet surface during CME-like space weather conditions. IMF orientation: Exoplanet-star (red line) and southward (green line). The horizontal dashed lines indicate the SW dynamic pressure at different exoplanet orbits: 2.5 au (orange) and 5.0 au (blue). The critical IMF intensity is indicated for each IMF orientation.

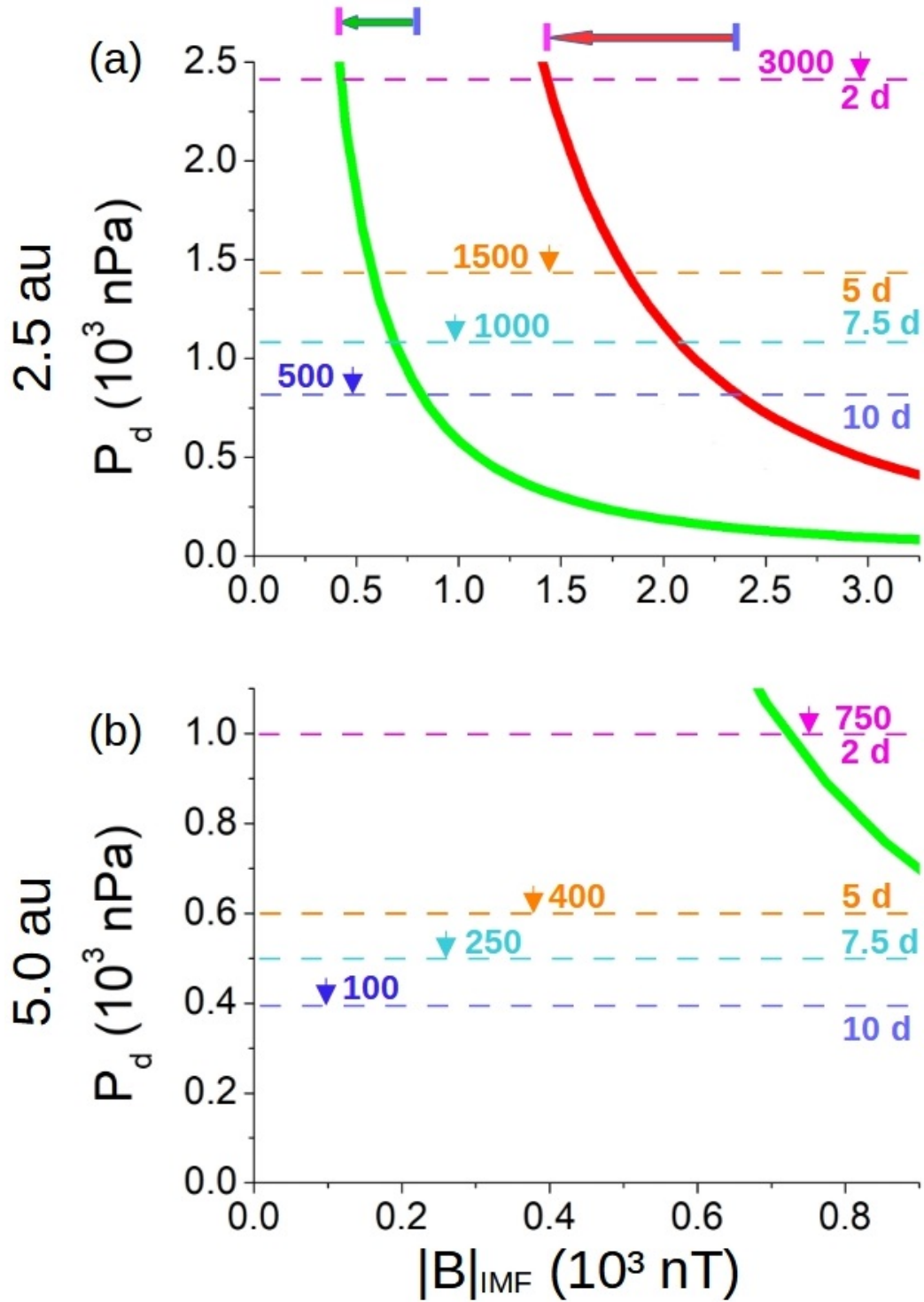


Figure 4. Critical IMF intensity and dynamic pressure required for the direct precipitation of the SW considering different F star rotation periods and exoplanets located at 2.5 au (a) and 5.0 au (b) orbits. IMF orientation: Exoplanet-star (red line) and southward (green line). The horizontal dashed lines indicate the SW dynamic pressure for F stars with rotation periods: 10 days (blue), 7.5 days (light cyan), 5 days (orange) and 2 days (pink). The bold colored arrows show the decrease of the critical IMF intensity required for the direct SW deposition if the F star rotation increases from 10 to 2 days. The green (red) color of the bold arrow indicates a southward (exoplanet-star) IMF orientation. The tentative critical IMF intensity is indicated for each star rotation rate.

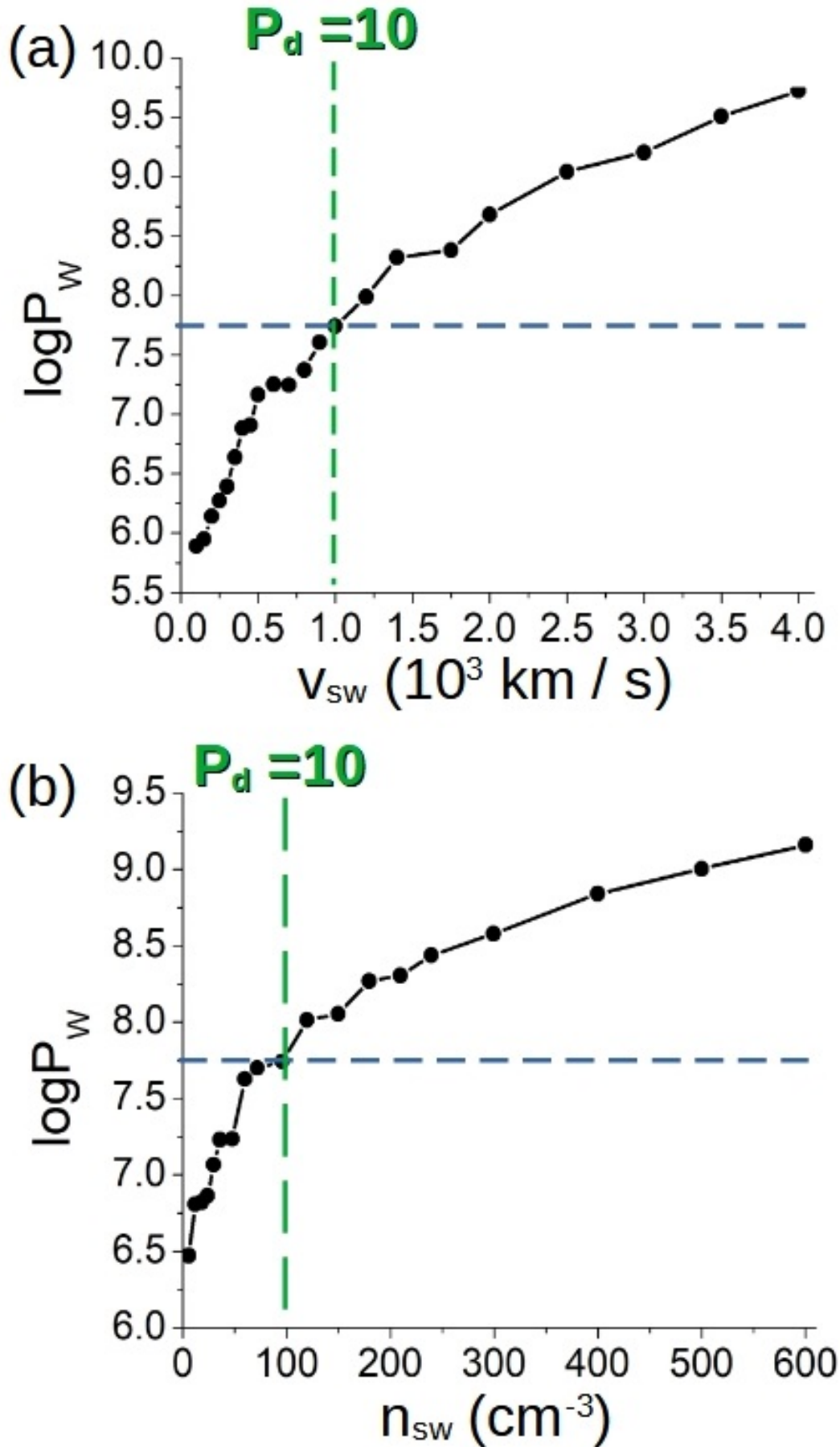


Figure 5. Radio emission power generated in the ²⁹day side of the exoplanet magnetosphere for a star-exoplanet IMF orientation with $|B|_{IMF} = 10$ nT if (a) the SW density is fixed to 12 cm^{-3} and the SW velocity changes and (b) the SW velocity fixed to 350 km/s and the SW density changes. The blue dashed horizontal line indicate the radio emission derived from the scaling law by ? (?). The green dashed vertical line indicates the simulations with $P_d = 10$ nPa.

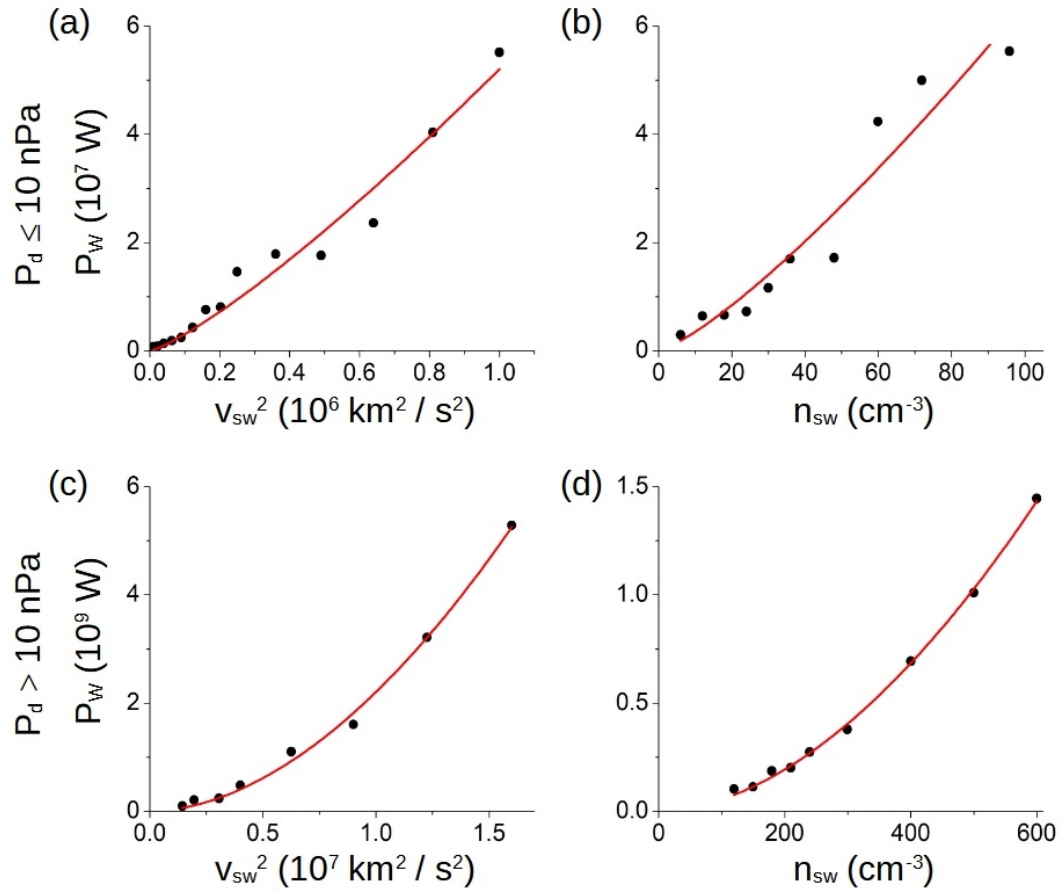


Figure 6. Data regression of the radio emission with respect to the square value of the SW velocity for (a) $P_d \leq 10$ and (c) $P_d > 10$. Data regression of the radio emission with respect to the SW density for (b) $P_d \leq 10$ and (d) $P_d > 10$.

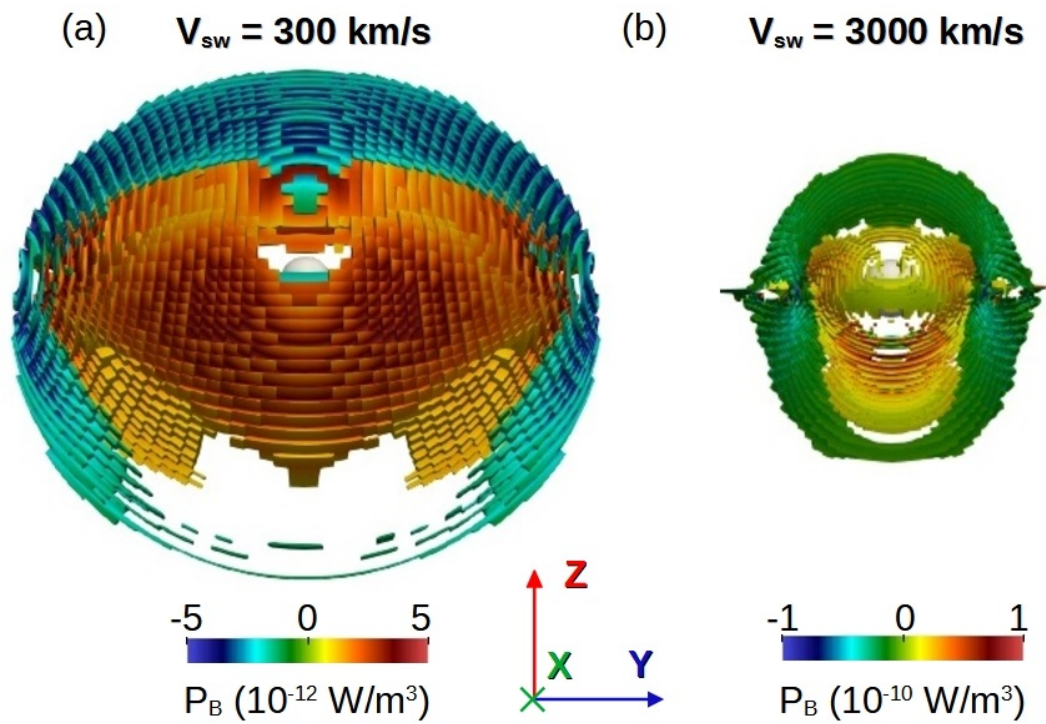


Figure 7. Iso-volume of the Poynting flux divergence in the bow shock and magnetopause region for simulations with (a) $v_{sw} = 300 \text{ km/s}$ and (b) $v_{sw} = 3000 \text{ km/s}$. Star-exoplanet IMF orientation with $|B|_{IMF} = 10 \text{ nT}$ and SW density of 12 cm^{-3} . Both panels show plots with the same dimensional scale.

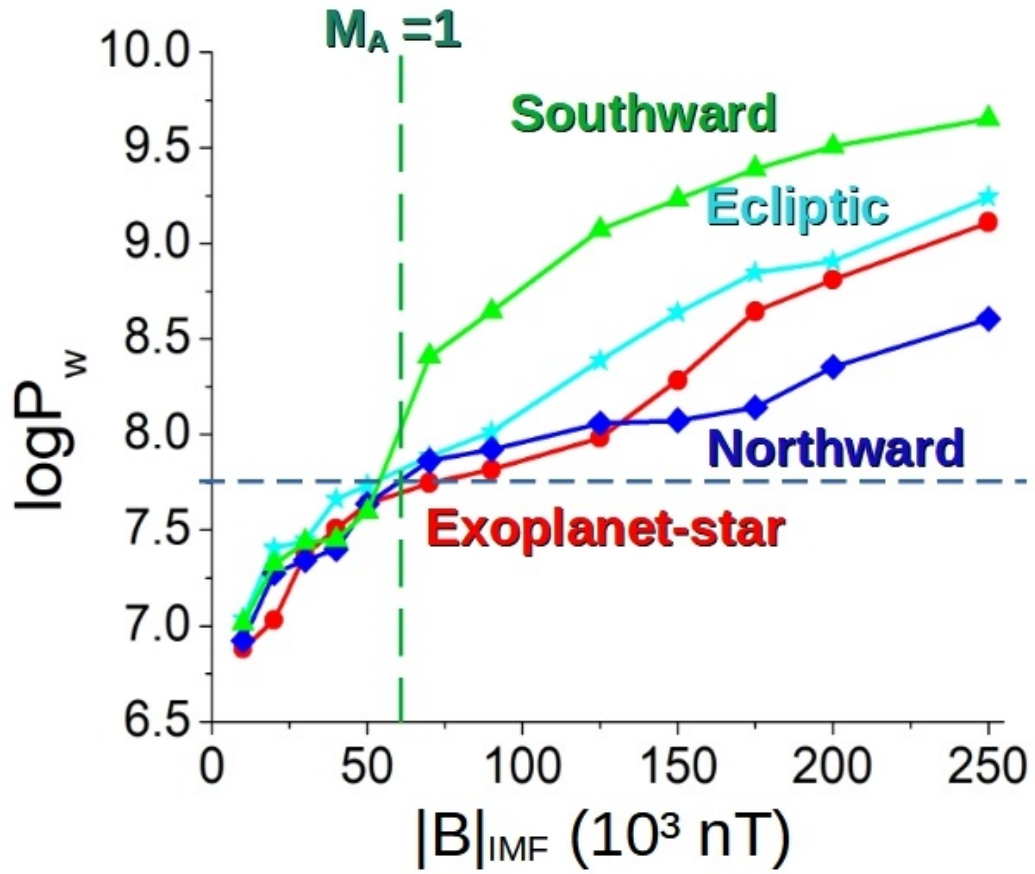


Figure 8. Logarithm of the radio emission power for simulations with $P_d = 1.2$ nPa and $|B|_{IMF} = 10 - 250$ nT. IMF orientations: Exoplanet-star (red dots), northward (blue diamonds), southward (green triangle) and ecliptic (cyan stars). The blue dashed horizontal line indicate the radio emission range derived from the scaling law by (?). The dark green dashed vertical line indicates the simulations with $M_A < 1$ (right) and $M_A > 1$ (left).

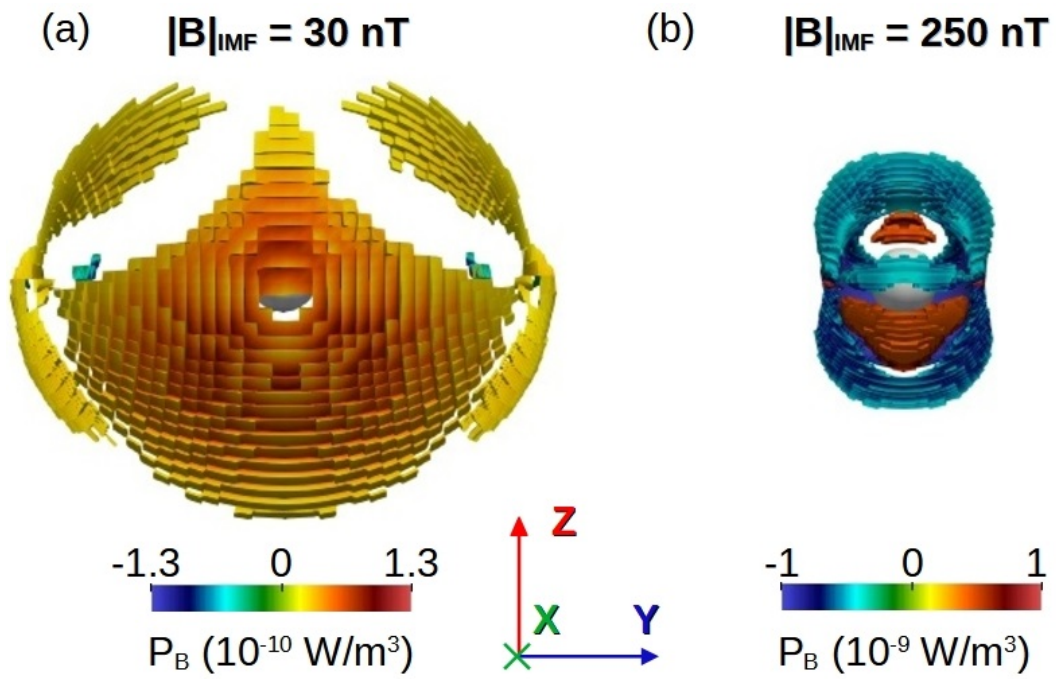


Figure 9. Iso-volume of the Poynting flux divergence in the bow shock and magnetopause region for simulations with (a) $|B|_{IMF} = 30 \text{ nT}$ and (b) $|B|_{IMF} = 250 \text{ nT}$. Exoplanet-star IMF orientation and $P_d = 1.2 \text{ nPa}$. Both panels show plots with the same dimensional scale.

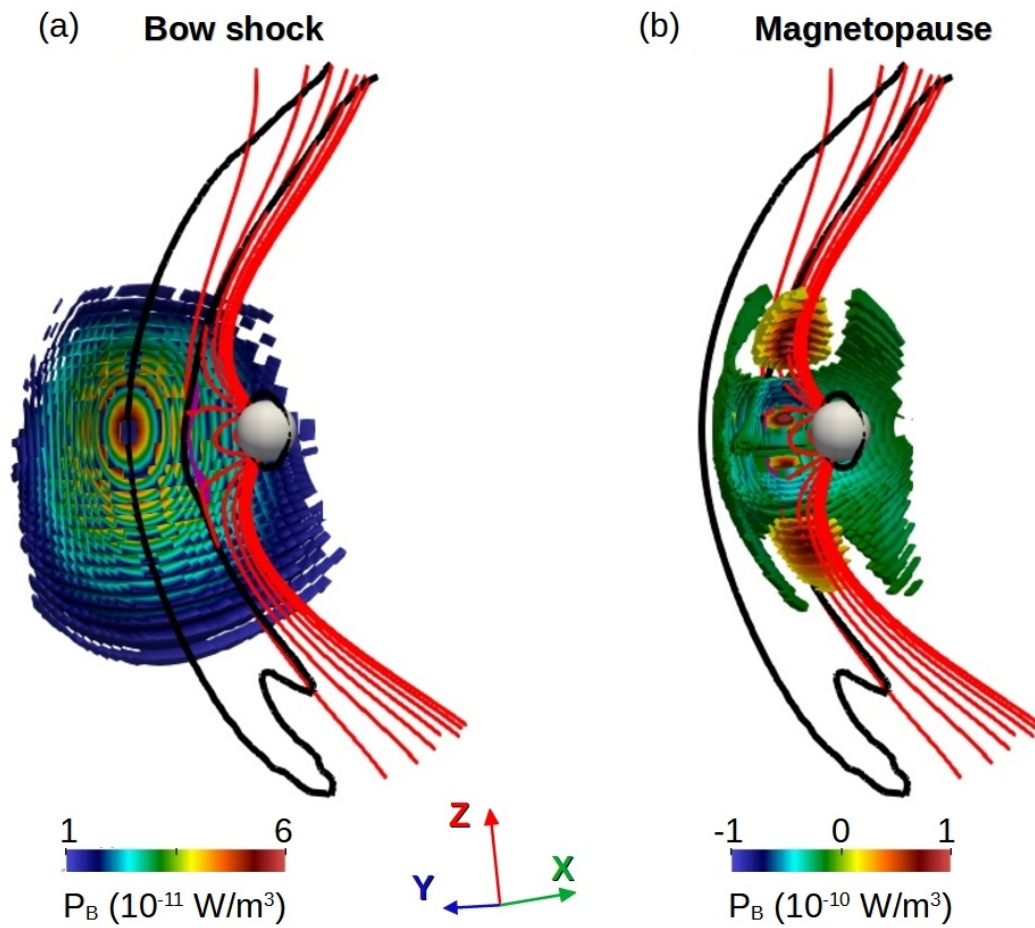


Figure 10. Poynting flux divergence in (a) the bow shock nose and (b) magnetopause reconnection regions. Simulation with southward IMF orientation, $|B|_{IMF} = 30 \text{ nT}$ and $P_d = 1.2 \text{ nPa}$. Black lines indicate the region of the bow shock ($n > 20 \text{ cm}^{-3}$), the red lines the exoplanet magnetic field lines and the pink iso-surface the reconnection region in the XZ plane ($|B| < 5 \text{ nT}$).

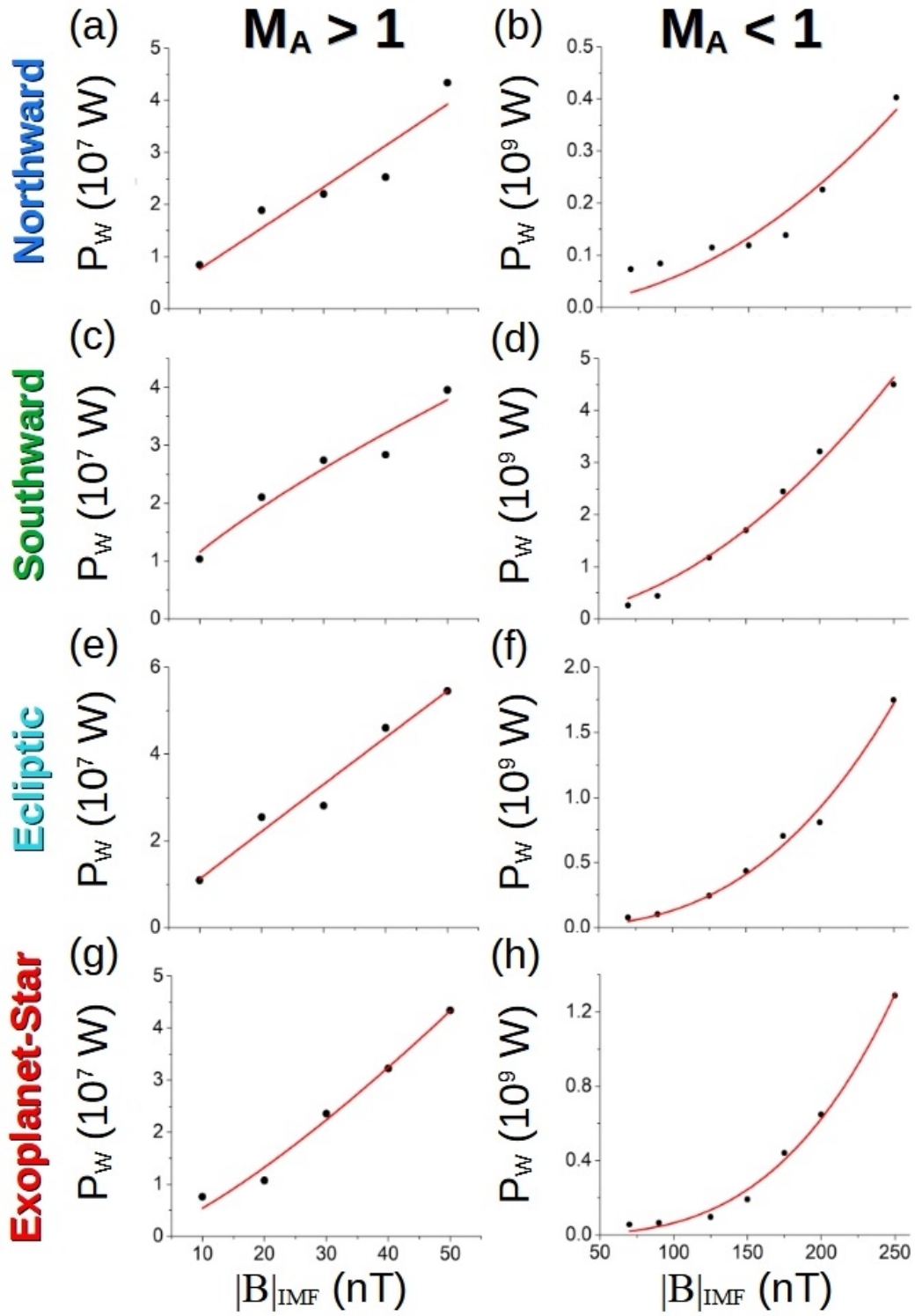


Figure 11. Data fit of the regression $P_w \approx \Gamma|B|_{sw}^\alpha$ if $|B|_{sw} < 70$ for (a) northward, (c) southward, (e) ecliptic and (g) exoplanet-star IMF. Same data regression if $|B|_{sw} \geq 70$ for (b) northward, (d) southward, (f) ecliptic and (h) exoplanet-star IMF.

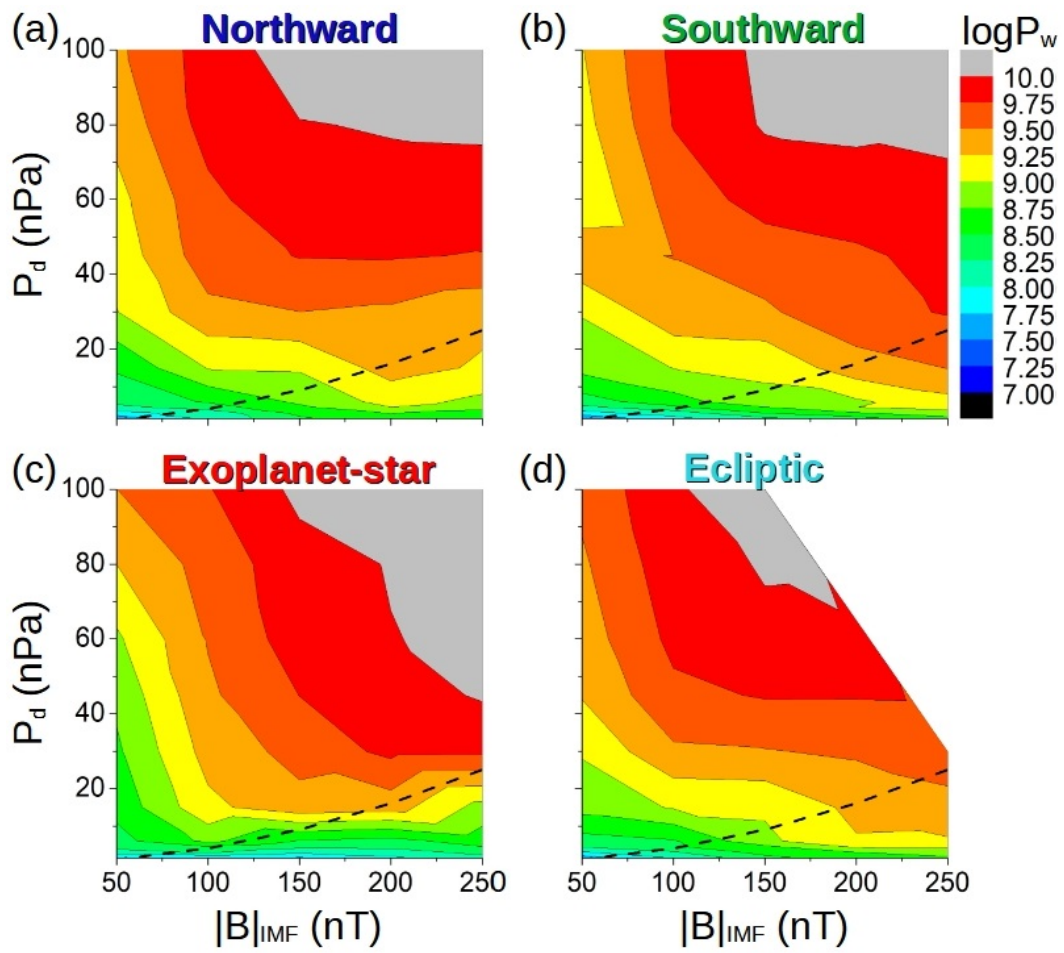


Figure 12. Logarithm of the radio emission with respect to the SW dynamic pressure and IMF intensity for (a) northward, (b) southward, (c) exoplanet-star and (d) ecliptic orientation. The dashed black line indicates the simulations with dominant SW pressure (above the line) and dominant IMF pressure (below the line).

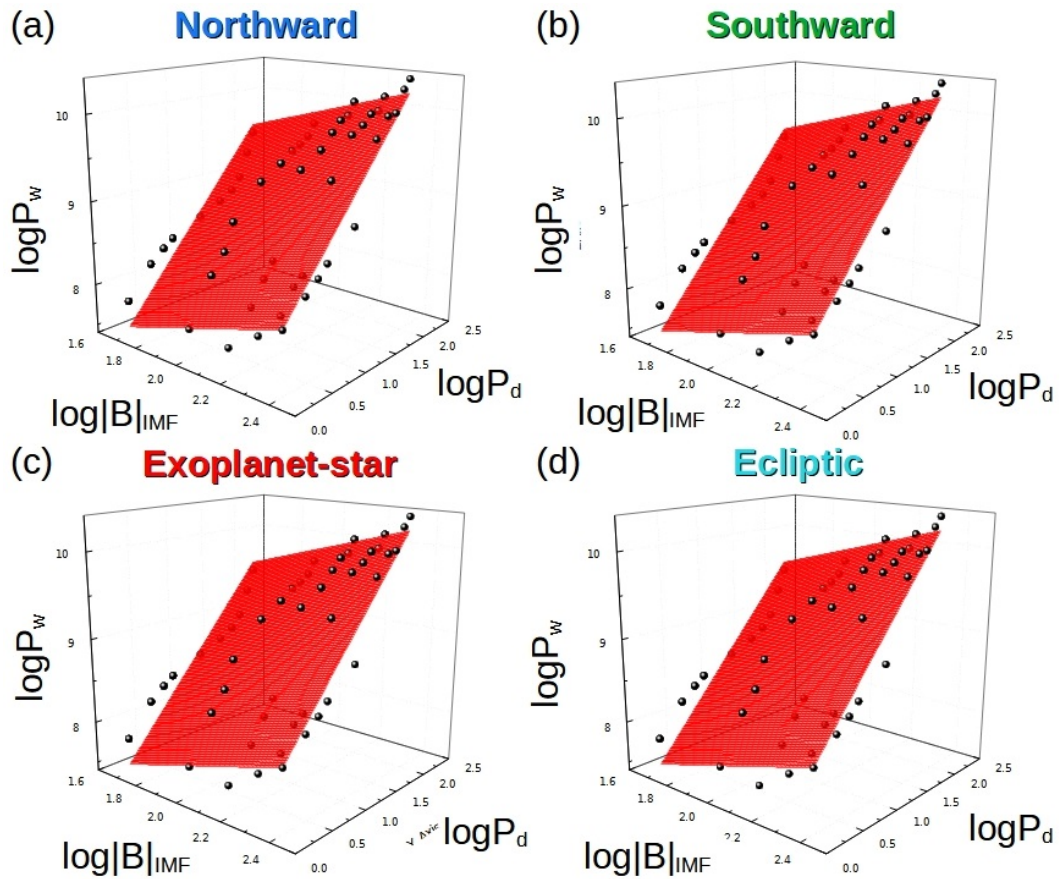


Figure 13. Data fit of the regression $\log P_w \propto \log Z + M \log |B|_{IMF} + N \log (P_d)$ for (a) northward, (b) southward, (c) exoplanet-star and (d) ecliptic IMF.

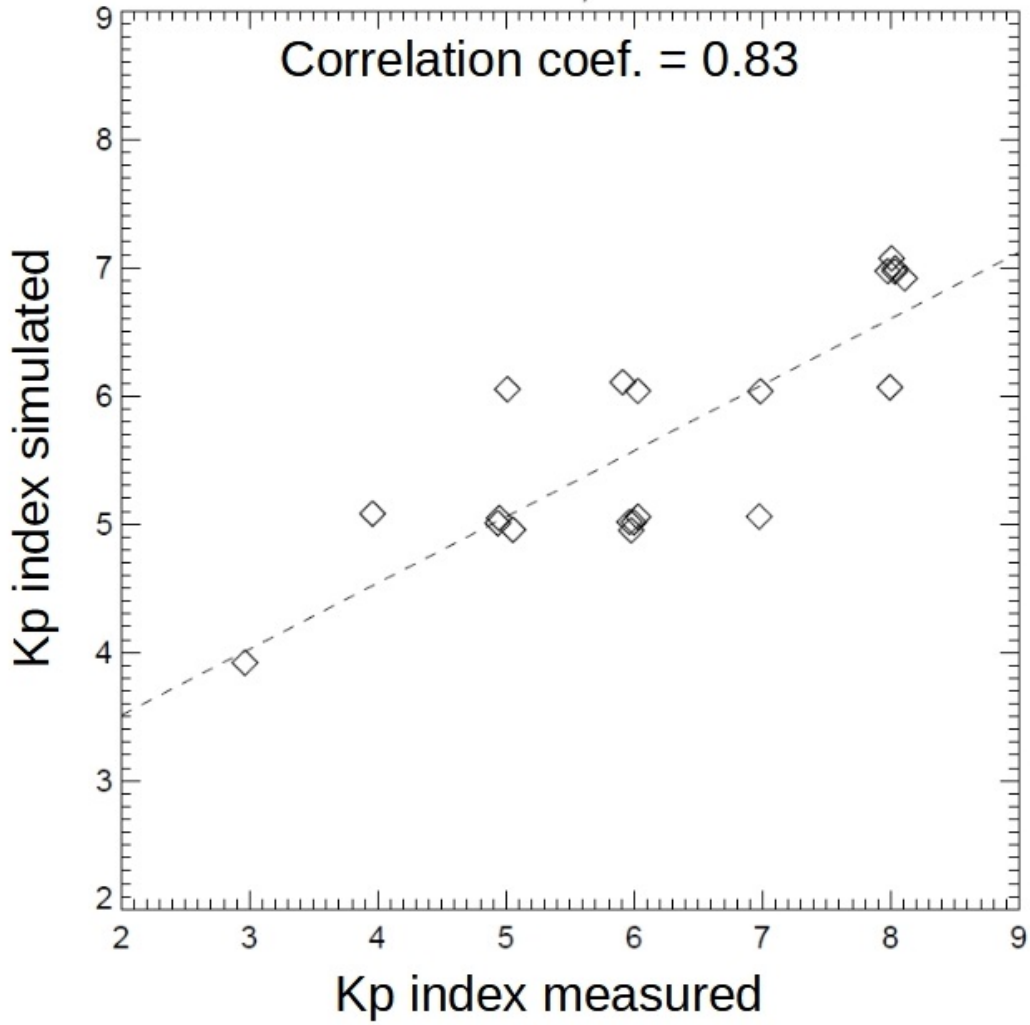


Figure A1. Correlation between the K_p index obtained in the simulations with respect to the measured values.